Experiments in Fluids 25 (1998) 409–430 © Springer-Verlag 1998

Accuracy of out-of-plane vorticity measurements derived from in-plane velocity field data

A. Fouras, J. Soria

Abstract A study of the errors in out-of-plane vorticity (ω_z) calculated using a local χ^2 fitting of the measured velocity field and analytic differentiation has been carried out. The primary factors of spatial velocity sampling separation and random velocity measurement error have been investigated. In principle the ω_z error can be decomposed into a bias error contribution and a random error contribution. Theoretical expressions for the transmission of the random velocity error into the random vorticity error have been derived. The velocity and vorticity field of the Oseen vortex has been used as a typical vortex structure in this study. Data of different quality, ranging from exact velocity vectors of analytically defined flow fields (Oseen vortex flow) sampled at discrete locations to computer generated digital image frames analysed using cross-correlation DPIV, have been investigated in this study. This data has been used to provide support for the theoretical random error results, to isolate the different sources of error and to determine their effect on ω_z measurements. A method for estimating *in-situ* the velocity random error is presented. This estimate coupled with the theoretically derived random error transmission results for the χ^2 vorticity calculation method can be used *a priori* to estimate the magnitude of the random error in ω_z. This random error is independent of a particular flow field. The velocity sampling separation is found to have a profound effect on the precise determination of ω_z by introducing a bias error. This bias error results in an underestimation of the peak vorticity. Simple equations, which are based on a local model of the Oseen vortex around the peak vorticity region, allowing the prediction of the ω_z bias error for the χ^2 vorticity calculation method, are presented. An important conclusion of this study is that the random error transmission factor and the bias error cannot be minimised simultaneously. Both depend on the velocity sampling separation, but with opposing effects. The application of the random and bias vorticity error predictions are illustrated by application to experimental velocity data determined using cross-correlation DPIV (CCDPIV) analysis of digital images of a laminar vortex ring.

Received: 31 October 1997/Accepted: 6 February 1998

A. Fouras, J. Soria
Department of Mechanical Engineering
Monash University
Clayton, VIC, Australia

Correspondence to: J. Soria

The authors gratefully acknowledge the support of this research by an ARC grant. The authors are also greatly indebted to Mr J. Cater who undertook the vortex ring experiments and his many helpful suggestions and Mr. J. Kostas for his helpful comments.

1 Introduction

1.1 Velocity measurement

Optical instantaneous in-plane velocity vector field measurement methods are becoming standard experimental tools in many fundamental and applied fluid mechanics investigations. A variety of methods are available. Some of these methods have evolved directly out of flow visualisation methods, such as particle streak measurement techniques (or streak photography) (e.g. Dimotakis et al. 1981; Imaichi and Ohmi 1983) and particle tracking methods (e.g. Agui and Jimenez 1987), while some have their origins in solid surface motion measurement techniques, i.e. laser speckle velocimetry (LSV) (e.g. Baker and Fourney 1977; Simpkins and Dudderar 1978). Light sheets generated by short duration illumination sources (e.g. pulsed lasers) are used in most of these techniques to freeze the motion of seed particles in the plane of interest. A derivative of LSV in particle image velocimetry (PIV). In this method distinct seed particle images are photographically recorded rather than their speckle interference pattern (Adrian 1986).

PIV is becoming the method of choice for many experimental fluid mechanics investigations requiring velocity vector field data. Multi-exposed image acquisition of flow planes with autospectrum or auto-correlation PIV analysis has been used for more than a decade in many fluid mechanics investigations (e.g. Simpkins and Dudderar 1978; Adrian and Yao 1985; Shepherd et al. 1991; Arroyo and Saviron 1992; Wu et al. 1994). This method cannot unambiguously determine the direction of recirculating flow (i.e. the vector direction) without sophisticated image shifting between the multiple exposures. It also has limitations in respect to the smallest velocity magnitude which can be measured. These problems do not exist in methods which use single exposed sequential frames in conjunction with cross-correlation digital PIV analysis. The limitations of this latter approach are only due to currently available hardware technology. The cross-correlation PIV analysis algorithm uses the normalised spatial cross-correlation

function, defined as

$$\rho(\Delta x, \Delta y) = \frac{\langle I_{s1}(i, j)\, I_{s2}\ (i-\Delta x, j-\Delta y)\rangle}{\sqrt{\langle I_{s1}^2(i, j)\rangle}\ \sqrt{\langle I_{s2}^2(i, j)\rangle}} \tag{1}$$

to determine the local velocity within a sampling window. Let I_{s1} and I_{s2} represent an interrogation window of size $Lx \times Ly$ pixels^2 (px^2) that is extracted from two sequential digital image frames. The $\langle\ \rangle$ symbol represents the discrete correlation operator. The location of the maximum in the normalised spatial cross-correlation function represents the average displacement of all particles within the sampling window. This location is found to sub-pixel accuracy using a least-square fit to a two-dimensional Gaussian function using all the information available around the peak of the cross-correlation function (Soria 1996). The complete in-plane velocity field is determined by sweeping the sampling window through the entire image frame.

This type of PIV algorithm is able to resolve displacements of 0.1 ± 0.06 px at the 95% confidence level (Soria 1996). Examples of experimental hardware implementations and applications of cross-correlation digital PIV (CCDPIV) to instantaneous in-plane velocity vector field measurements in unsteady fluid flow are found in Willert and Gharib (1991), Graham and Soria (1994) and Soria (1996).

This paper deals with the accuracy of derived quantities from planar velocity fields, specifically the accuracy of the out-of-plane vorticity distribution. Although presently instantaneous planar velocity field measurements are predominantly determined experimentally using a version of PIV, the analysis and the results of the out-of-plane vorticity inaccuracies discussed in this paper do not rely on any particular velocity field measurement procedure. In other words, the results pertaining to the accuracy analysis of out-of-plane vorticity distribution measurements presented in this paper are independent of the in-plane velocity field measurement procedure or the type of in-plane velocity measurements. With respect to the latter the results apply equally well to instantaneous vorticity distributions determined from instantaneous velocity fields or to mean vorticity distributions determined from mean velocity field data.

The necessary pieces of information for the analysis and discussion presented in this paper are: (a) an estimate of the magnitude of the random velocity error and (b) the spatial sampling separation between the velocity measurements. The velocity measurement uncertainty is assumed to have a Gaussian distribution and is therefore characterised by the standard deviation of the velocity field measurements. The use of the Gaussian noise model for the random velocity measurement error is reasonable as shown for PIV measurements by Soria (1996). In this study the standard deviation of the velocity measurements is assumed to be isotropic and spatially homogeneous with the same value for both orthogonal velocity components, i.e.

$$\sigma_u \equiv \sigma(u(X, Y)) = \sigma(v(X, Y)) \tag{2}$$

where $\sigma(u(X, Y))$ and $\sigma(u(X, Y))$ denote the standard deviation of the $u(X, Y)$ and $v(X, Y)$ velocity component measurements respectively and (X, Y) represents a global in-plane Cartesian coordinate set.

Unequal standard deviations representing unequal magnitudes of random error in the two orthogonal velocity component measurements can be easily accounted for by defining a new parameter Σ as the ratio of the standard deviations of $u(X, Y)$ and $v(X, Y)$ and carrying this parameter through the entire analysis, i.e.

$$\Sigma \equiv \frac{\sigma(u)}{\sigma(v)}$$

$$\sigma_u \equiv \sigma(u)$$

and

$$\sigma(v) = \sigma_u / \Sigma$$

Here the dependence on (X, Y) has been omitted to make it explicit that the standard deviations of $u(X, Y)$ and $v(X, Y)$ are independent of (X, Y), but are not equal. Although the present study is restricted to $\Sigma = 1$, it should be noted, that the analysis and final results presented in Sect. 3.1 can be easily modified to account for this additional parameter.

A final point to note is that the various sources of random error related to experimental apparatus and instrumentation, that lead to the random velocity measurement error are not within the scope of this paper and are therefore not discussed.

1.2 Vorticity measurement

The vorticity field, $\boldsymbol{\omega}$, is an important Gallilean invariant vector field. Each of the vorticity components can be computed from correspondingly measured in-plane velocity vector field data using its basic definition, i.e

$$\boldsymbol{\omega} = \nabla \times \mathbf{u} \tag{3}$$

where $\mathbf{u}$ is the velocity vector field. This paper is concerned with the measurement of one component, denoted by ω_z and which is pointing in the positive Z-direction of an X–Y–Z Cartesian coordinate frame, i.e.

$$\omega_z = \frac{\partial v}{\partial X} - \frac{\partial u}{\partial Y} \tag{4}$$

where u and v are the velocity components in the X- and Y-directions of the X–Y–Z coordinate frame respectively. The results derived in this paper apply equally well to the remaining vorticity components ω_x and ω_y pointing in the X- and Y-directions respectively.

The accuracy of the ω_z field measurement depends primarily on the spatial sampling distance between the velocity data points (i.e. the spatial resolution between the in-plane velocity vector samples) and on the accuracy of the velocity vector field measurements. In turn, these two factors depends on the measurement method employed to measure the velocity vector field samples. For example, in the image acquisition phase of PIV some of the factors which affect the velocity measurement accuracy are: (i) the imaging spatial resolution (e.g. lines/mm or pixel/mm), (ii) the ratio of seed particle diameter to vorticity distribution length scale and (iii) the seeding density.

In addition, the ω_z measurement accuracy is dependent on the computational method used to calculate it from the measured in-plane velocity vector field data. Sinha and

Kuhlman (1992) in considering this question investigated the relative accuracy of using: (i) the adaptive Gaussian window (AGW) interpolator proposed in the work of Agui and Jimenez (1987) with finite differencing to calculate the in-plane velocity gradients and hence, vorticity and (ii) a multiquadratic interpolator with analytic differentiation to obtain the vorticity. Their study showed that the latter method was the more accurate. Spedding and Rignot (1993) came to a similar conclusion in a study in which they compared the performance of different grid interpolation techniques, finding that a two-dimensional thin-shell spline interpolation with analytic differentiation outperformed the AGW interpolation with finite differencing. It is worth noting that Agui and Jimenez (1987) already remarked that the best results were obtained using certain polynomial least square interpolation rather than AGW with finite differencing, although no further details and no data substantiating this remark were presented.

Neither Sinha and Kuhlman (1992) nor Spedding and Rignot (1993) considered in their studies of vorticity accuracy, the vorticity error introduced due to velocity sampling separation or the inter-relationship between the velocity sampling separation and the random velocity error. In this respect important considerations are: (i) the accuracy with which ω_z can be determined relative to a known $\omega_{z_{\text{exact}}}$ using a given calculation procedure and (ii) the factors which affect this accuracy.

The error introduced into ω_z can be decomposed into a bias component, denoted by ω_{bias} and a random component, denoted by ω_z', such that

$$\omega_z(X,\ Y) = \omega_{z_{\text{exact}}}(X,\ Y) + \omega_{\text{bias}}(X,\ Y) + \omega_z'(X,\ Y) \tag{5}$$

In other words the expected value of $\omega_z(X, Y)$ for a number of *equivalent* experimental realisations is given by

$$E[\omega_z(X,\ Y)] = \omega_{z_{\text{exact}}}(X,\ Y) + \omega_{\text{bias}}(X,\ Y) \tag{6}$$

where $E[\cdot]$ denotes the expected value operator. The expected value of $\omega_z'(X, Y)$ is therefore given as

$$E[\omega_z'(X,\ Y)] = 0 \tag{7}$$

The random uncertainty in the ω_z measurement is characterised by the variance of ω_z', i.e. $\sigma^2(\omega_z')$. Note that from Eq. (5) and Eq. (6) the variance of ω_z is then given as

$$\sigma^2(\omega_z) = \sigma^2(\omega_z') \tag{8}$$

In general, the covariance between two random variables A and B is defined as

$$\sigma(A\ B) = E[(A-\mu_A)\ (B-\mu_B)] \tag{9}$$

where

$$\mu_A \equiv E[A]$$

and

$$\mu_B \equiv E[B]$$

are the mean of the random variables A and B respectively. If $A = B$ then

$$\sigma_A^2 \equiv \sigma^2(A) \equiv \sigma(A\ A) = E[A\ A] \tag{10}$$

Assuming that the in-plane velocity components $u(X, Y)$ and $v(X, Y)$ are independent random variables, then $\partial v/\partial X$ and $\partial u/\partial Y$ are also independent random variables. Using Eq. (9) it can then be shown that the variance of ω_z is given by

$$\sigma^2(\omega_z) = \sigma^2\left(\frac{\partial v}{\partial X}\right) + \sigma^2\left(\frac{\partial u}{\partial Y}\right) \tag{11}$$

It is readily noticed that a similar argument leads to relationships between the variances of $\partial v/\partial X$, i.e. $\sigma^2(\partial v/\partial X)$, and of $\partial u/\partial Y$, i.e. $\sigma^2(\partial u/\partial Y)$ and the random uncertainty in the velocity measurement of $u(X, Y)$ and $v(X, Y)$, characterised by their respective variances $\sigma^2(u(X, Y))$ and $\sigma^2(v(X, Y))$. Thus, in respect to the random uncertainty in vorticity measurements, the problem can be stated as one of finding the relationship between the uncertainty in the vorticity and the uncertainty in the velocity as a function of the vorticity calculation method. In other words, what is the form of the dimensional function $\mathscr{F}$ (Vorticity Calculation Methods), i.e.

$$\frac{\sigma^2(\omega_z)}{\sigma_u^2} = \mathscr{F}\ (\text{Vorticity Calculation Method})$$

Note that the assumed conditions imposed on the uncertainty of the velocity as stated in Sect. 1.1 have been implemented in this functional equation.

A corresponding dimensionless and thus more useful result is the ratio of normalised random vorticity error, i.e. $\sigma_{\omega_z}/(V_{\text{ref}}/L)$, to the normalised random velocity error, i.e. σ_u/V_{ref}, where V_{ref} is a characteristic velocity scale and L is a characteristic length scale. Defining this dimensionless ratio as λ_0, it can be shown that

$$\lambda_0 = \frac{\sigma(\omega_z)}{V_{\text{ref}}/L} \div \frac{\sigma_u}{V_{\text{ref}}} = L\,\frac{\sigma(\omega_z)}{\sigma_u} \tag{12}$$

The ratio given by Eq. (12) is also the ratio of the non-dimensional standard deviations of the non-dimensionalised ω_z vorticity component and the non-dimensional (u, v) velocity components. This can easily be shown by noting that if ω_z and (u, v) are non-dimensionalised by V_{ref}, the characteristic velocity scale, and L, the characteristic length scale, such that

$$u^* = \frac{u}{V_{\text{ref}}}, \qquad v^* = \frac{v}{V_{\text{ref}}}, \qquad \omega_z^* = \frac{\omega_z}{V_{\text{ref}}/L}$$

where the superscript "*" denotes the non-dimensional variables and the spatial dependence is assumed but not explicitly shown, then the non-dimensional standard deviations of (u^*, v^*) and ω_z^* are given as

$$\sigma^*(u) = \sqrt{E\ [(u^* - E[u^*])^2]} = \frac{\sigma(u)}{V_{\text{ref}}}$$

$$\sigma^*(v) = \sqrt{E\ [(v^* - E[v^*])^2]} = \frac{\sigma(v)}{V_{\text{ref}}}$$

$$\sigma^*(\omega_z) = \sqrt{E\ [(\omega_z^* - E[\omega_z^*])^2]} = \frac{\sigma(\omega_z)}{V_{\text{ref}}/L}$$

Hence,

$$\lambda_0 \equiv \frac{\sigma^*(\omega_z)}{\sigma_u^*} \tag{13}$$

where $\sigma_u^* \equiv \sigma^*(u) = \sigma^*(v)$.

λ_0 can therefore be thought of as a natural non-dimensional random error transmission ratio.

The effect of the zero-mean random velocity error and spatial velocity samples separation on each of these error components and on the non-dimensional error transmission ratio, λ_0 will be analysed and their implications are discussed in the remainder of this paper, Although a number of results pertaining to the AGW-FD method are also developed and presented for comparison, the primary focus of this analysis is on the χ^2 velocity fit-analytic differentiation method described in Sect. 3.

2 The adaptive Gaussian window-finite difference out-of-plane vorticity calculation method

The basis of the adaptive Gaussian window-finite difference (AGW-FD) method for calculating out-of-plane vorticity from in-plane velocity is reviewed here for completeness, as the errors in the vorticity using this method are compared to those of the χ^2 velocity fit-analytic differentiation method described in Sect. 3. Further details and a more thorough discussion of this method can be found in the papers of Agui and Jimenez (1987), Sinha and Kuhlman (1992) and Spedding and Rignot (1993). The original ideal of the adaptive Gaussian window (AGW) was as an interpolator of randomly located velocity samples derived from particle tracking onto a regular rectangular grid prior to the application of a finite difference (FD) scheme to determine ω_z. In the present study the velocity samples are assumed to be available on a regular grid, with $(\tilde{u}(X_l', Y_m'), \tilde{v}(X_l', Y_m'))$ representing the in-plane velocity samples at the point (X_l', Y_m'). It should be noted at this point, that most of the fundamental concepts and framework developed in this paper do not require this restriction, and apply equally well to randomly located velocity samples which are then characterised by a *mean* velocity sampling separation or distance.

Due to the assumption in the present development of regularly spaced data on a rectangular grid, the AGW interpolator acts only as a smoothing filter, i.e.

$$u(X_i', Y_j') = \frac{\sum_{l,m} \alpha_{lm}\, \tilde{u}(X_l', Y_m')}{\sum_{l,m} \alpha_{lm}}$$

$$v(X_i', Y_j') = \frac{\sum_{l,m} \alpha_{lm}\, \tilde{v}(X_l', Y_m')}{\sum_{l,m} \alpha_{lm}} \tag{14}$$

where

$$\alpha_{lm} = \exp\left(\frac{-\{[X_i' - X_l']^2 + [Y_j' - Y_m']^2\}}{H^2}\right) \tag{15}$$

and (u, v) denote the smoothed in-plane velocity components at each of the regular rectangular grid points (X_i', Y_i'). The value of H determines the width of the Gaussian function and hence, controls the amount of smoothing. The optimum value for H was found by Agui and Jimenez (1987) to be 1.24Δ, where in the original context of particle tracking, Δ was defined as the mean particle separation. In the present context, Δ is defined as the velocity sampling separation. In all results pertaining to the application of AGW-FD in the present study, $H = 1.24\Delta$ was used.

The out-of-plane vorticity can be computed directly using the velocity samples on the regular rectangular grid points with the following central finite difference formula:

$$\omega_z(X, Y) = \frac{v(X+h_x, Y) - v(X-h_x, Y)}{2h_x} - \frac{u(X, Y+h_y) - u(X, Y-h_y)}{2h_y} \tag{16}$$

where h_x and h_y are the displacements of the velocity sampling points in the x and y directions respectively. In general they do not have to be equal and do not have to be equal to Δ, the original velocity sampling distance. However, in this study the following restriction is applied, $h_x = h_y = \Delta$ and hence,

$$\omega_z(X, Y) = \frac{v(X+\Delta, Y) - v(X-\Delta, Y) - u(X, Y+\Delta) - u(X, Y-\Delta)}{2\Delta} \tag{17}$$

The random error transmission from the sampled velocity uncertainty to the ω_z uncertainty can be theoretically computed, and is thus available *a priori*. The relationship between λ_0 and Δ/L for vorticity calculations using the finite difference method without prior AGW velocity field smoothing is calculated in a straightforward manner using the uncertainty analysis presented in Sect. 1.2 (or see Moffat 1988). This results in

$$\lambda_0 = \frac{1}{\Delta/L} \tag{18}$$

The theoretical prediction of the relationship between λ_0 and Δ/L for the full AGW-FD vorticity calculation method can also be developed using uncertainty analysis, but involves significantly more algebra. The following relationship, which only applies to sampled velocity data on a regular rectangular grid (e.g. as shown in Fig. 1) has been deduced,

$$\lambda_0 = \frac{1}{\Delta/L}\,[W(N, M)]^{1/2} \tag{19}$$

where

$$W(N, M) = \frac{\sum_{n=-N}^{n=N} \sum_{m=-M}^{m=M} \exp\left(\frac{-2(n^2+m^2)}{1.24}\right)}{\left[\sum_{n=-N}^{n=N} \sum_{m=-M}^{m=M} \exp\left(\frac{-(n^2+m^2)}{1.24}\right)\right]^2}$$

and N, M denote the extent of discrete data which is used to calculate the AGW smoothed velocity field. The results in Table 1 show how $W(N, M)$ varies for different values of N and M. Using the results presented in this table and considering that more than 3 sample points in all directions are used to AGW smooth the velocity field prior to FD vorticity calculation results in the following non-dimensional relationship for the

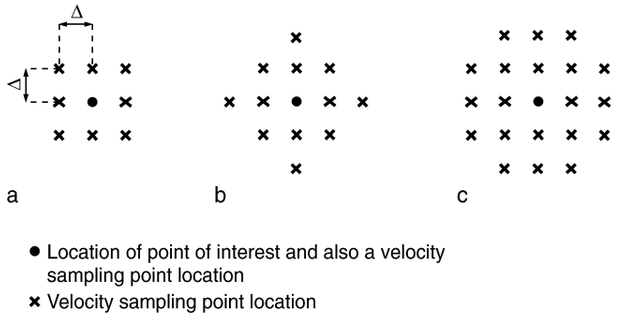

Fig. 1a–c. Rectangular grid patterns used for the calculation of ω_z using the χ^2 method. The locations of the velocity sampling points and the point of interest relative to the velocity sampling points are identified for. **a** The χ^2_9 method which uses 9 velocity sampling points; **b** the χ^2_{13} method which uses 13 velocity sampling points and **c** the χ^2_{21} method which uses 21 velocity sampling points

Table 1. Relationship between number of sampled velocity points used in AGW velocity smoothing and $W(N, M)$

N	M	$W(N, M)$
1	1	0.1368
1	2	0.1197
2	2	0.1048
2	3	0.1043
3	3	0.1037
∞	∞	0.1037

random error transmission in the AGW-FD vorticity calculation method,

$$\lambda_0 = \frac{0.3220}{\Delta / L} \tag{20}$$

Comparison with Eq. (18) shows analytically that the AGW-FD vorticity calculation method results in a lower transmission of the velocity random error into the random ω_z error than the FD vorticity calculation method without prior AGW smoothing of the velocity field.

3 The χ^2 velocity fit-analytic differentiation out-of-plane vorticity calculation method

A second order polynomial χ^2 fit to the two orthogonal in-plane velocity components with analytic differentiation as outlined in Soria (1996) is used in the present study. The in-plane velocity vector field is assumed to be available at a discrete number of points (X_i, Y_i) in the form of the horizontal and vertical velocity components, $\tilde{u}(X_i, Y_i)$ and $\tilde{v}(X_i, Y_i)$. The subscript "i" denotes the ith sampling point. The nearest N sampling data points to the point of interest are selected for the calculation of the out-of-plane vorticity component, ω_z. The mean separation distance between these points is denoted by Δ, the spatial sampling separation of the velocity data. For example, in PIV measurements the sampling points are usually on a regular Cartesian grid and hence, Δ is in this case the shortest distance between two neighbouring points.

The sampled in-plane velocity components $\tilde{u}(x_i, y_i)$ and $\tilde{v}(x_i, y_i)$ are separately fitted to a polynomial of Kth power in x and y using a χ^2 procedure (Press et al. 1989). The linear combination of the polynomials requires $M = (K+1)^2$ coefficients. Thus, the number of data points, N, required for the χ^2 fitting process is $N \geqslant M$.

An important point to note is that the coordinates (x, y) denoted a *local* Cartesian coordinate set with its origin at the point of interest (X, Y) in the global Cartesian coordinate set. The interpolated in-plane velocity components and the out-of-plane vorticity at the point of interest (X, Y) are thus given as

$$u(X, Y) = u(x = 0, y = 0)$$

$$v(X, Y) = v(x = 0, y = 0)$$

and

$$\omega_z(X, Y) = \omega_z(x = 0, y = 0)$$

This χ^2 fitting procedure results in two polynomial functions for the local in-plane velocity components $u(x, y)$ and $v(x, y)$ of the form

$$u(x, y) = \sum_{i=0}^{M-1} u_i \times X_i(x, y) \tag{21}$$

$$v(x, y) = \sum_{i=0}^{M-1} v_i \times X_i(x, y) \tag{22}$$

$X_i(x, y)$ are given polynomial basis functions. It is straightforward to analytically differentiate these expressions to obtain

$$\frac{\partial u}{\partial y}(x, y) = \sum_{i=0}^{M-1} u_i \times \frac{\partial X_i}{\partial y}(x, y) \tag{23}$$

and

$$\frac{\partial v}{\partial x}(x, y) = \sum_{i=0}^{M-1} v_i \times \frac{\partial X_i}{\partial x}(x, y) \tag{24}$$

The out-of-plane vorticity $\omega_z(x, y)$ is then given by

$$\omega_z(x, y) = \sum_{i=0}^{M-1} \left(v_i \times \frac{\partial X_i(x, y)}{\partial x} - u_i \times \frac{\partial X_i(x, y)}{\partial y} \right) \tag{25}$$

after noting that a translation of the Cartesian axis from the global frame $(X, Y) \rightarrow$local frame (x, y) does not affect the spatial derivatives, i.e.

$$\frac{\partial}{\partial x} = \frac{\partial}{\partial X}, \qquad \frac{\partial}{\partial y} = \frac{\partial}{\partial Y}$$

The polynomial basis functions $X_i(x, y)$ used in this study comprise the set:

$$X_i(x, y) \in \{1, x, x^2, y, y^2, xy, x^2y, xy^2, x^2y^2\} \tag{26}$$

This set of basis functions is formally not of Kth order in x and y, but only $K = 2$ in x and $K = 2$ in y. This results in $M = 9$, i.e. 9 coefficients need to be fitted to determine the local velocity

description. This process requires $N \geqslant 9$ velocity sampling points around the point of interest in the flow field.

Two comments are appropriate at this stage. The first comment relates to other basis functions such as sinusoids or Chebyshev functions which might be more appropriate in certain applications. The majority of the analytic framework and the analytic results developed in the following Sect. 3.1 makes no reference to any particular set of basis functions and thus, are independent of particular basis function sets. It is only the final results presented in Sect. 3.1 which specifically relate to the particular basis functions described by Eq. (26). The other comment relates to the spatial location of the sampled data points. Again the majority of the analytic framework and the analytic results developed in the following Sect. 3.1 make no reference to either structured regular grid or unstructured grids with randomly located sampling points, as for example found in particle tracking velocimetry. Hence, the analytic framework and the general results developed in the following section apply to any data, be it spatially located on a structured grid or located randomly. It is only the final results presented in Sect. 3.1 which specifically relate to data which is available on a structured rectangular grid.

3.1 Theoretical analysis of the random error in the χ^2 vorticity calculation method

The random error component in ω_z is a result of the random measurement error in the velocity data. In this section the propagation of this random velocity error into ω_z using the vorticity calculation method outlined in the previous Sect. 3 is analysed.

As already indicated, the in-plane velocity **V**, measured for example using a technique such as PIV is assumed to have a Gaussian random error described by the standard deviations $\sigma(u)$ and $\sigma(v)$ of the measured horizontal and vertical velocity components u and v respectively. It is evident from Eq. (25) that the means of propagation of the random error introduced by the velocity measurements into ω_z is only via the polynomial coefficients, as the derivatives of $X_i(x, y)$ are calculated exactly.

Considering the u_i coefficients calculated from the χ^2 fit to the u velocity component to be random variables, then their independence is described by the matrix $\mathbf{C_u}$ (Press et al. 1989).

$$\mathbf{C_u} = \sigma(u_i\ u_j) \tag{27}$$

where $\sigma(u_i u_j)$ is the covariance between u_i and u_j. The matrix $\mathbf{C_u}$ is related to a matrix A_{uij} which is defined as

$$A_{uij} = \frac{X_j(x_i,\ y_i)}{\sigma(u)} \tag{28}$$

where (x_i, y_i) identifies the local coordinates of the ith sampling data point. $\sigma(u)$ is the standard deviation representing the random error associated with the u velocity component measurement which is assumed to have the same value for all the sampling data points. A positive definite matrix $\mathbf{\Lambda_u}$ can be defined as

$$\mathbf{\Lambda_u} = \mathbf{A_u^T} \cdot \mathbf{A_u} \tag{29}$$

and it can be shown (Press et al. 1989) that the matrix $\mathbf{C_u}$ in Eq. (27) is given as

$$\mathbf{C_u} = \mathbf{\Lambda_u^{-1}} \tag{30}$$

The diagonal elements of $\mathbf{C_u}$ represent the variances $\sigma(u_i\ u_i)$ of the fitted parameters u_i. If the off-diagonal elements of $\mathbf{C_u}$ representing the covariances between u_i and u_j are zero, then the fitted parameters u_i are independent.

A similar analysis results in the matrix $\mathbf{C_v} = \sigma(v_i\ v_j)$ for the coefficients v_i calculated from a χ^2 fit to the v velocity component.

Now, using Eq. (9) the variance of $\partial v/\partial x$ is given by

$$\sigma^2\left(\frac{\partial v}{\partial x}\right) = E\left[\left(\frac{\partial v}{\partial x} - \mu\left(\frac{\partial v}{\partial x}\right)\right)^2\right] \tag{31}$$

substituting Eq. (24) for $\partial v/\partial x$ yields

$$\sigma^2\left(\frac{\partial v}{\partial x}\right) = E\left[\left\{\sum_{i=0}^{M-1}\left(v_i \times \frac{\partial X_i(x,\ y)}{\partial x} - \mu\left(\frac{\partial v}{\partial x}\right)\right)\right\}^2\right]$$

or

$$\sigma^2\left(\frac{\partial v}{\partial x}\right) = E\left[\left(\sum_{i=0}^{M-1}(\gamma_i - \mu(\gamma_i))\right)^2\right] \tag{32}$$

where $\gamma_i = v_i \times \partial X_i(x, y)/\partial x$. Since the summation and expected value operators commute

$$\sigma^2\left(\frac{\partial v}{\partial x}\right) = \sum_{i=0}^{M-1}\sum_{j=0}^{M-1} E\left[(\gamma_i - \mu_{\gamma_i})(\gamma_j - \mu_{\gamma_j})\right] \tag{33}$$

and noting that

$$\mu_{\gamma_i} = \mu\left(\frac{\partial v}{\partial x}\right) = E\left[\sum_{i=0}^{M-1} v_i \times \frac{\partial X_i(x,\ y)}{\partial x}\right]$$

$$= \sum_{i=0}^{M-1} \frac{\partial X_i(x,\ y)}{\partial x} E[v_i]$$

$$= \sum_{i=0}^{M-1} \mu(v_i) \frac{\partial X_i(x,\ y)}{\partial x}$$

results in

$$\sigma^2\left(\frac{\partial v}{\partial x}\right) = \sum_{i=0}^{M-1}\sum_{j=0}^{M-1} E\left[\left(\{v_i - \mu(v_i)\} \times \frac{\partial X_i(x,\ y)}{\partial x}\right) \times \left(\{v_j - \mu(v_j)\} \times \frac{\partial X_j(x,\ y)}{\partial x}\right)\right] \tag{34}$$

i.e.

$$\sigma^2\left(\frac{\partial v}{\partial x}\right) = \sum_{i=0}^{M-1}\sum_{j=0}^{M-1}\left(\frac{\partial X_i(x,y)}{\partial x}\frac{\partial X_j(x,y)}{\partial x} E\left[(v_i - \mu(v_i))(v_j - \mu(v_j))\right]\right) \tag{35}$$

Once again using Eq. (9) yields

$$\sigma^2\left(\frac{\partial v}{\partial x}\right)=\sum_{i=0}^{M-1}\sum_{j=0}^{M-1}\left(\frac{\partial X_i(x,\ y)}{\partial x}\frac{\partial X_j(x,\ y)}{\partial x}\sigma(v_i\ v_j)\right) \tag{36}$$

or using the corresponding form of Eq. (27) results in the following expression for the variance of $\partial v/\partial x$:

$$\sigma^2\left(\frac{\partial v}{\partial x}\right)=\sum_{i=0}^{M-1}\sum_{j=0}^{M-1}\left(\frac{\partial X_i(x,\ y)}{\partial x}\frac{\partial X_j(x,y)}{\partial x}C_{vij}\right) \tag{37}$$

A similar analysis results in the variance of $\partial u/\partial y$ given by

$$\sigma^2\left(\frac{\partial u}{\partial y}\right)=\sum_{i=0}^{M-1}\sum_{j=0}^{M-1}\left(\frac{\partial X_i(x,\ y)}{\partial y}\frac{\partial X_j(x,y)}{\partial y}C_{uij}\right) \tag{38}$$

Adding Eqs. (37) and (38) as required by Eq. (11) results in the variance of ω_z

$$\sigma^2(\omega_z)=\sum_{i=0}^{M-1}\sum_{j=0}^{M-1}\left(\frac{\partial X_i(x,y)}{\partial x}\frac{\partial X_j(x,y)}{\partial x}C_{vij}+\frac{\partial X_i(x,y)}{\partial y}\frac{\partial X_j(x,y)}{\partial y}C_{uij}\right) \tag{39}$$

Recalling that

$$C_{uij}=\Lambda_{uij}^{-1}\quad\text{where }\Lambda_{uij}=\frac{\Lambda_{ij}}{\sigma^2(u)}$$

and

$$C_{vij}=\Lambda_{uij}^{-1}\quad\text{where }\Lambda_{vij}=\frac{\Lambda_{ij}}{\sigma^2(v)}$$

where

$$\Lambda_{ij}=\sum_{k=1}^{N}X_j(x_k,\ y_k)\ X_i(x_k,\ y_k) \tag{40}$$

Thus, using the assumption described by Eq. (2) which implies that

$$\Lambda_{uij}=\Lambda_{vij}=\frac{\Lambda}{\sigma_u^2} \tag{41}$$

and furthermore defining

$$C_{ij}=\Lambda_{ij}^{-1} \tag{42}$$

results in

$$C_{uij}=C_{vij}=\sigma_u^2\,C_{ij} \tag{43}$$

The variance of ω_z is therefore given by

$$\sigma^2(\omega_z)=\sigma_u^2\sum_{i=0}^{M-1}\sum_{j=0}^{M-1}C_{ij}\left(\frac{\partial X_i}{\partial x}\frac{\partial X_j}{\partial x}+\frac{\partial X_i}{\partial y}\frac{\partial X_j}{\partial x}\right) \tag{44}$$

A transmission factor, $K_\varepsilon(x,\ y)$, describing the effects of velocity random error on the vorticity measurements can be defined as

$$K_\varepsilon(x,\ y)\equiv\frac{\sigma^2(\omega_z)}{\sigma_u^2} \tag{45}$$

which after using Eq. (44), becomes the following expression:

$$K_\varepsilon(x,\ y)=\sum_{i=0}^{M-1}\sum_{j=0}^{M-1}C_{ij}\left(\frac{\partial X_i(x,y)}{\partial x}\frac{\partial X_j(x,y)}{\partial x}+\frac{\partial X_i(x,y)}{\partial y}\frac{\partial X_j(x,y)}{\partial y}\right) \tag{46}$$

The units of K_ε are (Length)$^{-2}$. It is noted from the equation above, that $K_\varepsilon(x,\ y)$ is only a function of the spatial derivatives $\partial X_i(x,\ y)/\partial x$ and $\partial X_i(x,\ y)/\partial y$ and the matrix **C**. The matrix **C** is in turn only a function of the data distribution and the given basis functions $X_i(x,\ y)$. Thus, it can be summarised that $K_\varepsilon(x,\ y)$ is only dependent on:

1. K – the order of the given basis functions and their type;
2. The number and spatial distribution of data points around the point of interest used for the χ^2 interpolation.

Hence, for a given set of these parameters, a value of $K_\varepsilon^0=-K_\varepsilon(0,\ 0)$ can be determined at any point of interest in the flow field. However, as the local velocity is presumably fitted using the χ^2 method with the same interpolation basis functions $X_i(x,\ y)$ and using the same parameters around each local point of interest, it is concluded that the calculated value of K_ε^0, given by

$$K_\varepsilon^0=K_\varepsilon(0,\ 0)=\sum_{i=0}^{M-1}\sum_{j=0}^{M-1}C_{ij}\left(\frac{\partial X_i(0,\ 0)}{\partial x}\frac{\partial X_j(0,\ 0)}{\partial x}+\frac{\partial X_i(0,\ 0)}{\partial y}\frac{\partial X_j(0,\ 0)}{\partial y}\right) \tag{47}$$

is independent of the global position within the flow field, and hence independent of any particular flow and can therefore be represented by a single scalar value. This value provides all the required information of the propagation of the *local* velocity random error into the *local* vorticity random error for every point in the flow field and can be determined *a priori* before any measurements are performed. This allows Eq. (47) to be used as a experimental design tool to estimate the propagation of velocity random error to vorticity random error. Equation (47) provides a method for the determination of the expected variance of the random error in ω_z due to the random measurement error in the velocity field as characterised by its variance.

It must be re-iterated that no specific basis functions $X_i(x,y)$ have been applied to this point and no restriction on the spatial distribution of the velocity sample point has been imposed. Hence. Eq. (47) applies to any basis function set, besides the ones specified by Eq. (26) and to data which is available either on structured grids or unstructured grids with randomly positioned data points.

The theoretical results to be developed from this point onwards are calculated assuming that: (i) the basis functions are as specified by Eq. (26) and (ii) the velocity samples are available on a regular rectangular grid as shown in Fig. 1. Thus, any subsequent conclusions must be viewed in the light of these restrictions.

The use of the basis functions specified by Eq. (26) requires a minimum of 9 sample points. Furthermore, these sample points are assumed to be arranged as indicated in Fig. 1a. The corresponding spatial arrangement of 13 and 21 velocity

sample points is shown in Fig. 1b and (c) respectively. The following nomenclature is adopted to indicated the number of data points used for the χ^2 vorticity and uncertainty calculation:

1. χ^2_9 indicates 9 sampled points arranged as shown in Fig. 1a,
2. χ^2_{13} indicates 13 sample points arranged as shown in Fig. 1b and
3. χ^2_{21} indicates 21 sample points arranged as shown in Fig. 1c.

Equation (47) reduces to a summation of two terms for the basis functions given by Eq. (26), i.e.

$$K^0_\varepsilon = C_{11} + C_{33} \tag{48}$$

where the components of the matrix **C** are given by Eq. (42), i.e. C_{11} and C_{22} are a functions of the basis functions evaluated at the spatial positions of the velocity sampling points, K^0_ε has been computed in closed form for the spatial distributions of the data shown in Fig. 1 and for the different χ^2 vorticity calculation methods:

1. χ^2_9:

$$K^0_\varepsilon = \frac{1}{\Delta^2} \tag{49}$$

2. χ^2_{13}:

$$K^0_\varepsilon = \frac{1}{5}\frac{1}{\Delta^2} \tag{50}$$

3. χ^2_{21}:

$$K^0_\varepsilon = \frac{7}{65}\frac{1}{\Delta^2} \tag{51}$$

Figure 2 shows a graph of Eqs. (49)–(51), indicating that the negative exponent in these relationships is independent of the number of sampling points used to calculate K^0_ε (and ω_z). However, the coefficient multiplying this power law relation is found to depend on the number of sampling points used to calculate ω_z.

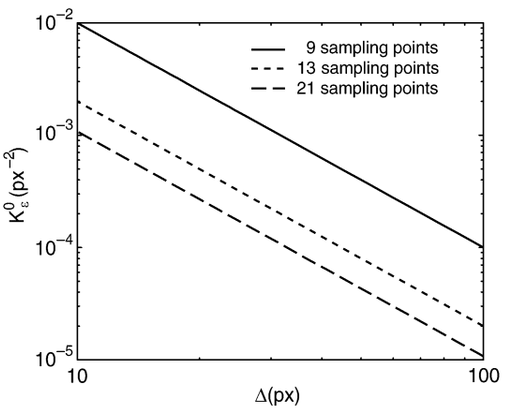

Fig. 2. Variation of K^0_ε with Δ for different number of sampling points used in the χ^2-ω_z calculation method

An interesting theoretical deduction is that the χ^2 vorticity calculation method can produce a variance in ω_z which is numerically smaller than the variance of the velocity measurement. For example, if the velocity samples are regularly distributed on a rectangular grid with a separation of $\Delta = 10$ px and ω_z is calculated using the χ^2_9 method, then $\sigma(\omega_z)$ is 10 times smaller than the standard deviation associated with the velocity measurement (i.e. σ_u). This example represents the worst case shown in Fig. 2, because due to the negative nature of the exponent in this power law relationship, the standard deviation in the vorticity is reduced by increasing the normalised spacing between the sampling points.

It can be shown, by combining Eqs. (12) and (45), that the relationship between λ_0 and K^0_ε is

$$\lambda_0 = \frac{\sigma(\omega_z)}{V_{\mathrm{ref}}/L} \div \frac{\sigma_u}{V_{\mathrm{ref}}} = L\sqrt{K^0_\varepsilon} \tag{52}$$

Therefore, the normalised transmission ratio of the vorticity random error is given via λ_0 by combining Eq. (52) with the appropriate equation for K^0_ε (i.e. one of Eqs. (49)–(51) depending of the specific χ^2_x vorticity calculation method employed). The value of λ_0 can be calculated *a priori* using one of the following appropriate theoretical relationships:

1. χ^2_9:

$$\lambda_0 = \frac{1}{\Delta/L} \tag{53}$$

2. χ^2_{13}:

$$\lambda_0 = \sqrt{\frac{1}{5}}\frac{1}{\Delta/L} \tag{54}$$

3. χ^2_{21}:

$$\lambda_0 = \sqrt{\frac{7}{65}}\frac{1}{\Delta/L} \tag{55}$$

The results of these theoretical predictions are shown as the lines in Fig. 3 for the χ^2_9, χ^2_{13} and χ^2_{21} vorticity calculation methods. These results, which are independent of location within the flow domain and independent of the flow at hand, show the inverse power law relationship between λ_0 and Δ/L. The multiplicative factor in this relationship is dependent on the number sample points and their spatial location.

Comparing the derived theoretical relationship between λ_0 and Δ/L for the χ^2_9 method (Eq. (53)) with the relationship derived in Sect. 2 for the FD method, i.e. Eq. (18), it is noted that the random error transmission characteristics of the FD method are identical to that of the χ^2_9 vorticity calculation method. Furthermore, solving analytically for ω_z $(x=0, y=0)$ given the 9 point grid used in the χ^2_9 method, it is found that ω_z $(x=0, y=0)$ is identically equal to the FD formula, i.e. Eq. (17), providing the explanation why the results of the χ^2_9 vorticity calculation method and the FD method are identical.

The multiplicative factor in Eq. (55), describing the relationship between λ_0 and Δ/L for the χ^2_{21} method is equal to 0.3282. Comparing the theoretical relationship between λ_0 and Δ/L for the AGW-FD vorticity calculation method, i.e. Eq. (20), with the result presented in Eq. (55), it is observed that the random

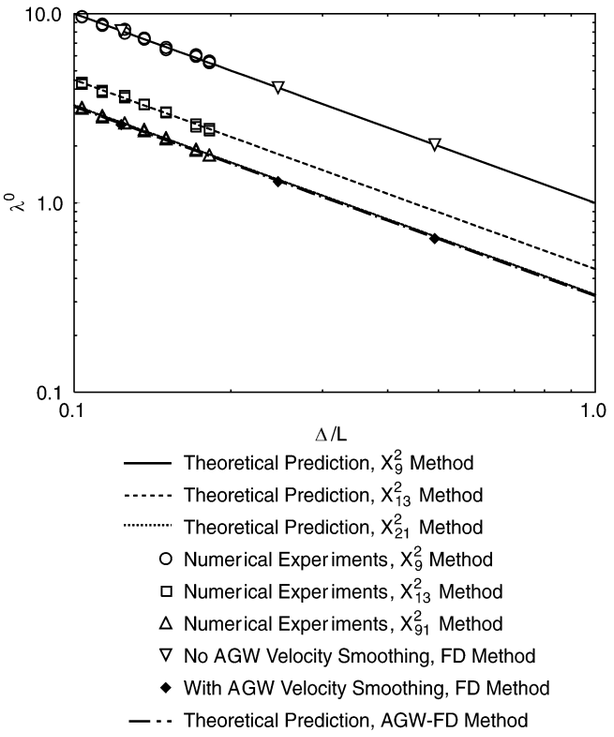

Fig. 3. Ratio of normalised vorticity standard deviation to normalised velocity standard deviation, i.e. λ_0, as a function of Δ/L. The solid lines are the theoretically predicted variations for vorticity calculated using the χ^2 method. The symbols are the vorticity results calculated using the χ^2 method from numerical experiments using noisy velocity data for the Oseen vortex flow field. Some corresponding results for vorticity calculated using the finite difference method without and with prior smoothing of the velocity field are also shown for comparison

error transmission characteristic of the χ^2_{21} vorticity calculation method is approximately equal to that of the AGW-FD vorticity calculation method. A graphical comparison of these results is shown in Fig. 3. This graph also shows that the χ^2_{13} vorticity calculation method has a random error transmission characteristic which is approximately 36% higher than the χ^2_{21} method but 55% lower than the χ^2_9 vorticity calculation method for a very small additional increase in computational cost. The theoretical prediction for the FD vorticity calculation methods is identical to the χ^2_9 vorticity calculation method.

To apply the results presented in Eqs. (53)–(55) to predict the random error in ω_z, an estimate of the random error in the velocity measurements is needed, i.e. an estimate of σ_u is required. The local χ^2 velocity fitting method can be used to arrive at an estimate for σ_u. The deviation of the fitted velocity from the measured velocity at the velocity sample point (X_i, Y_i) is defined as δu_i, i.e.

$$\delta u_i \equiv u(X_i, Y_i) - \tilde{u}(X_i, Y_i) \tag{56}$$

where

$$u(X_i, Y_i) = u(x=0, y=0) = \sum_{i=0}^{M-1} u_i \times X_i \ (x=0, y=0)$$

is the local χ^2 velocity fit evaluated at the sampling point which is identified in local coordinates by $(x=0, y=0)$ or in global coordinates by (X_i, Y_i). The expected value of this deviation and the expected value of the square of this deviation is computed using all the available in-plane velocity samples.

Numerical Monte Carlo simulations using analytically known velocity fields with superimposed Gaussian noise have shown that the expected value of the deviation is given as

$$E[\delta u_i] = 0$$

and that the expected value of the square deviation given by

$$\sigma^2_{\delta u} = E[\delta u_i^2] \tag{57}$$

is found to be directly proportional to σ_u, the standard deviation of the velocity random measurement error. The proportionality factor is found to be a weak function of Δ/L and can be assumed to be constant for $\Delta/L \leqslant 0.4$. But there is an unpredictable deviation of the proportionality factor for $\Delta/L > 0.4$. This is not unexpected, as the functional model using the basis functions given by Eq. (26) for the local velocity becomes an extremely *poor* model with increasing Δ/L. The characteristic length scale, L, is thought of here as the typical length scale over which there is a typical Δu variation. Identical statistical results are found for the other in-plane velocity component, $v(X, Y)$ and hence, both in-plane velocity components can be used to provide better statistics due to the doubling of the available samples.

The following relationships between σ_u and $\sigma_{\delta u}$ have been found when $\Delta/L \leqslant 0.4$:

1. χ^2_9:

$$\sigma_u = 1.493 \ \sigma_{\delta u} \tag{58}$$

2. χ^2_{13}:

$$\sigma_u = 1.190 \ \sigma_{\delta u} \tag{59}$$

3. χ^2_{21}:

$$\sigma_u = 1.124 \ \sigma_{\delta u} \tag{60}$$

The following procedure to estimate *a priori* the random error in ω_z depending on the specific χ^2_x vorticity calculation method used to calculate ω_z is thus proposed:

1. Calculate

$$\sigma^2_{\delta u} = \frac{E[\delta u_i^2] + E[\delta v_i^2]}{2}$$

where δu_i is given by Eq. (56) and δv_i is the corresponding deviation for $v(X, Y)$ given by an analogous equation to Eq. (56).

2. Calculate σ_u using the appropriate equation chosen from Eqs. (58)–(60) and non-dimensionalise using V_{ref} to arrive at σ^*_u.

3. Calculate λ_0 using the appropriate equation chosen from Eqs. (53)–(55).

4. Calculate $\sigma^*(\omega_z)$ using the definition of λ_0 (Eq. (13)) and the estimated value of σ^*_u.

4
Numerical experiments

Numerical experiments using an analytically known velocity field with a vorticity distribution representative of a typical vortex structure with a characteristic length scale were undertaken to: (i) study the effect of velocity sampling distance on the accuracy of the vorticity measurement, and (ii) provide supporting evidence for the theoretical results describing the transmission of random velocity error into random vorticity error. The flow field chosen for this study is the *Oseen Vortex* which is represented by an axisymmetric in-plane velocity field and out-of-plane vorticity distribution. The in-plane tangential velocity and out-of-plane vorticity field of the Oseen Vortex are given by Saffmann (1995) as

$$u_t(r) = \frac{\Gamma}{2\pi\tau}\left[1 - \exp\left(\frac{-r^2}{4\nu t}\right)\right] \tag{61}$$

$$\omega_z(r) = \frac{-\Gamma}{4\pi\nu\tau}\exp\left(\frac{-r^2}{4\nu t}\right) \tag{62}$$

where $r^2 = X^2 + Y^2$ and (X, Y) are global in-plane Cartesian coordinates, Γ is the circulation, ν is the kinematic viscosity and t is time. The instantaneous length scale L characterising the instantaneous size of the Oseen vortex is defined as

$$L \equiv \sqrt{2\nu t} \tag{63}$$

Numerical experiments have been performed with various values of L. The results presented here are predominantly for $L = 130$ px, as all results normalised by L collapse onto the results presented for $L = 130$ px.

To investigate the effect of the different sources of error, the accuracy of the vorticity measurements is examined at several levels of velocity data quality. These range from exact velocity field data, to exact velocity field data with superimposed Gaussian noise of varying standard deviations (i.e. different values of σ_u).

The accuracy of the χ^2 vorticity calculation procedures using the velocity measurement errors associated with one of the possible velocity field measurement techniques, namely cross-correlation DPIV (CCDPIV) analysis of digital particle images, was also investigated. In this part of the study, computer generated artificial PIV images representing the Oseen Vortex flow field were used to determine the velocity field.

4.1
Bias error-effect of velocity sampling separation

The results presented in Fig. 4 show the ω_z error distribution normalised by the known exact peak vorticity at $r = 0$ for noise-free velocity data. The results presented in Fig. 4 are arrived at by first calculating the exact noise-free velocity data which is locally discretised with a normalised spatial sampling separation Δ/L around the r/L point of interest. The vorticity, ω_z, is then calculated using the techniques outlined in Sects. 2 and 3. i.e. the FD vorticity calculation method (without prior AGW velocity field smoothing), the AGW-FD vorticity calculation method (with prior AGW velocity field smoothing) and the χ^2_9, χ^3_{13} and χ^2_{21} vorticity calculation methods. Subsequently, the vorticity error, which is identified from Eq. (6) as being the bias error, ω_{bias}, is calculated and graphed as a function of normalised radial position. Hence, the results in Fig. 4 illustrate solely the effect of the normalised spatial sampling separation of the velocity data, i.e. Δ/L, on the accuracy of the vorticity calculation.

Figure 4a and b show the bias vorticity error for the FD method without prior AGW velocity field smoothing and with prior AGW velocity field smoothing, respectively. The results presented in Fig. 4c–e correspond to the χ^2_9, χ^2_{13} and χ^2_{21} vorticity calculation method, respectively. The exact vorticity distribution is represented in Fig. 4 by a horizontal line crossing the zero value on the vertical axis. This data shows the significant effect that increasing Δ/L has on the magnitude of ω_{bias} and hence, the significant effect it has on the accuracy of vorticity determination.

The general observation in all vorticity calculation methods is a bias error found to result in: (i) an underestimate of the vorticity in the neighbourhood of the vortex core, i.e. $r/L \approx 1.5$ and (ii) a slight overestimate of the vorticity well away from the core, i.e. $r/L > 1.5$, this overestimation is found to asymptote to zero as the distance from the vortex centre increases. The largest underestimation of ω_z is not unexpectedly found at the vortex centre and is found to depend strongly on Δ/L. The smaller this value the smaller the vorticity bias error, ω_{bias}.

The neighbourhood of the peak ω_z region of the Oseen vortex represents a region of rapidly varying $u(X, Y)$ (i.e. large velocity gradients) and it is in this region where the bias error is largest. It is therefore easily concluded that the results presented in Fig. 4 are a manifestation of the spatial filter characteristics of each vorticity calculation method. As expected from the theoretical results developed in Sect. 3.1, the results presented in Fig. 4a for the FD vorticity calculation method and Fig. 4c for the χ^2_9 vorticity calculation method are identical, indicating identical spatial filter characteristics. Since it was shown that their random transmission characteristics are also equal, it is concluded that both these methods have nearly identical overall vorticity accuracy characteristics. The only practical advantage of using the χ^2_9 vorticity calculation method over the FD vorticity calculation method, is that the former provides an direct method for the evaluation of the vorticity anywhere within the local domain of the χ^2_9 velocity fit region.

From the results presented in Sect. 2, particularly comparing Eqs. (19) and (20), and as noted by previous investigators (Agui and Jimenez 1987; Sinha and Kulhman 1992; Spedding and Rignot 1993) AGW smoothing prior to FD vorticity calculation is desirable to minimise the random error transmission from velocity to vorticity. However, this practice results in quite a large increase in the vorticity bias error as shown in Fig. 4b. For $\Delta/L \leqslant 0.25$, Fig. 4b shows that the vorticity calculated using the full AGW-FD procedure results only in a bias underestimation of ω_z, i.e. no bias overestimation is observed far from the vortex core. Whereas for the $\Delta/L = 0.49$ case, bias overestimation of vorticity is observed far from the vortex centre. In summary, the lower random error transmission ratio, λ_0, found in the AGW-FD vorticity calculation method compared to the FD method comes at the cost of a significantly increased bias error which, as will be shown, is not found in the χ^2_{21} method for a similar random error transmission characteristic as the AGW-FD vorticity calculation method.

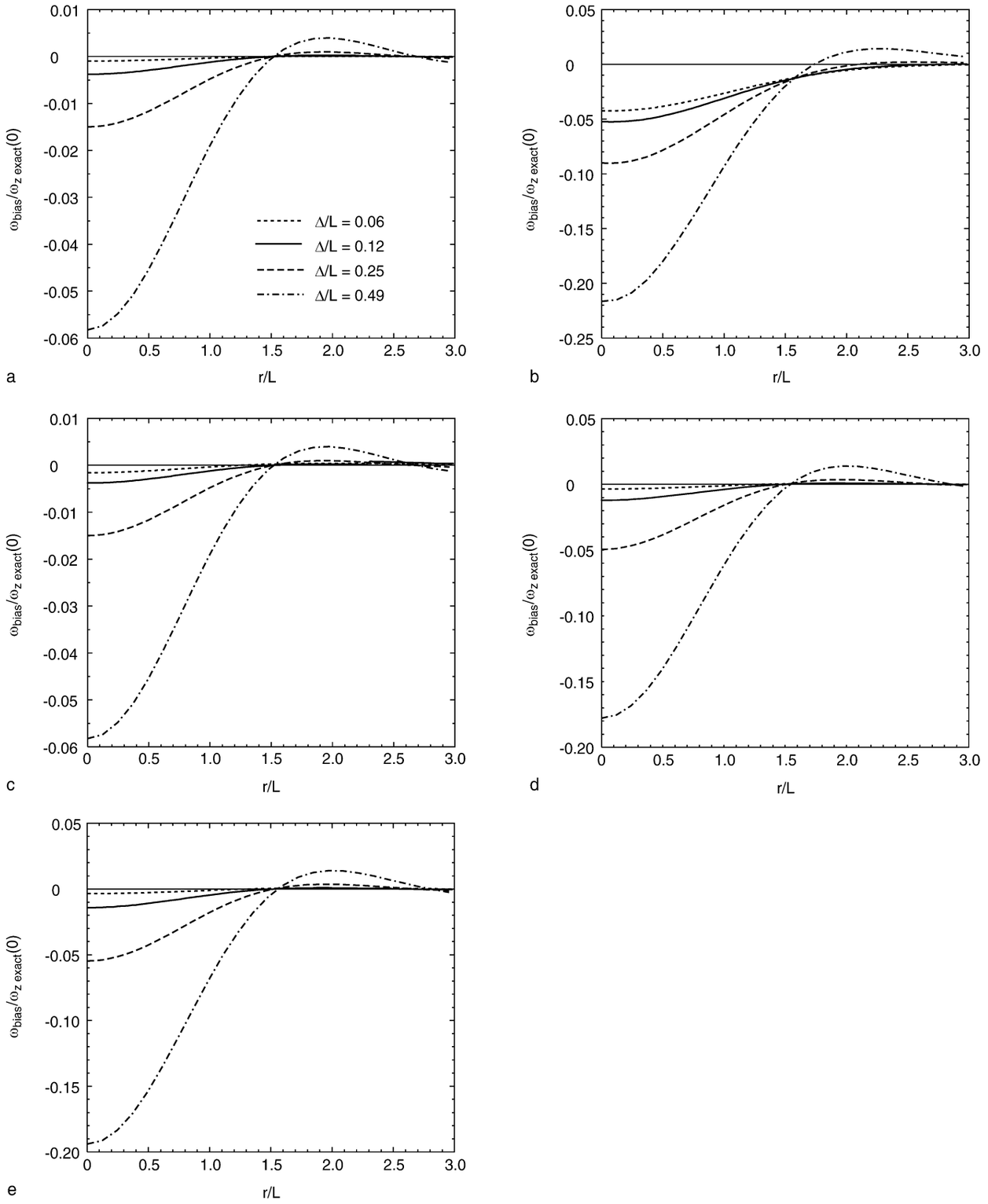

Fig. 4a–e. Bias error in ω_z calculation using exact discritised velocity data of the Ossen vortex for different Δ/L sampling separations and using different vorticity calculation methods. **a** Finite difference without prior AGW velocity field smoothing, **b** finite difference with prior AGW velocity field smoothing, **c** χ^2 method using 9 velocity sampling points, **d** χ^2 method using 13 velocity sampling points and **e** χ^2 method using 21 velocity sampling points

It is therefore worth comparing the bias error produced by the χ^2_{13} and χ^2_{21} vorticity calculation methods with that of the AGW-FD vorticity calculation method, as these two methods have considerably smaller velocity random error transmission than either the χ^2_9 or the equivalent FD vorticity calculation method (see Fig. 3). The bias error is considerably smaller for $\Delta/L \leqslant 0.25$ when using either the χ^2_{13} or the χ^2_{21} vorticity calculation methods compared to the corresponding AGW-FD vorticity bias error. In fact, using χ^2_{13} with $\Delta/L \approx 0.25$ gives a bias error similar to AGW-FD with $\Delta/L \approx 0.12$. In other words, only half the velocity sampling resolution for the same vorticity bias error is required if the χ^2_{13} vorticity calculation method is used compared to the AGW-FD method.

Overall, for all methods with $\Delta/L < 0.25$ the observed bias vorticity error provides on first sight an encouraging result. However, it is important to note that the cases which indicate a very small bias error, e.g. $\Delta/L = 0.05$, represent in practice the requirement for a large number of highly resolved velocity measurements across a vortex structure. This point is illustrated by considering the example where the velocity is sampled with $\Delta/L = 0.12$. In this case approximately 50 velocity measurements across a vortex structure are required to keep the maximum relative bias vorticity error below 2% (except for the AGW-FD method where $-\omega_{\text{bias}}(0)/\omega_{z_{\text{exact}}}(0) \approx 5\%$ for the same experimental conditions). The example shows that approximately 2500 velocity measurements on a regular rectangular grid covering the areas of a typical axisymmetric vortex structure are required, which implies a very stringent experimental requirement on the spatial resolution of the velocity sampling. In the case of image based velocimetry, this represents a high spatial resolution requirement of the image acquisition system.

The functional dependence of the normalised vortex centre vorticity bias error on Δ/L is shown in Fig. 5. This data shown that the functional dependence of the absolute normalised maximum bias error for the all χ^2 and the FD vorticity calculation methods is closely approximated by a quadratic power law over most of the Δ/L range shown in Fig. 5. The quadratic exponent is only a weak function of number of sampling points used in the χ^2 methods. However, the dependence on the number of sampling points is manifested in the coefficient multiplying the power law. The value of this coefficient is found to increase with number of sampling points and appears to asymptote to some value. Regression analysis assuming a power law for the χ^2 data shown in Fig. 5 results in the following relationships between the normalised peak bias vorticity error and the normalised velocity sampling separation, Δ/L:

1. χ^2_9

$$\frac{-\omega_{\text{bias}}(0)}{\omega_{z_{\text{exact}}}(0)} = 0.2416\left(\frac{\Delta}{L}\right)^{1.99} \tag{64}$$

2. χ^2_{13}

$$\frac{-\omega_{\text{bias}}(0)}{\omega_{z_{\text{exact}}}(0)} = 0.7478\left(\frac{\Delta}{L}\right)^{1.96} \tag{65}$$

3. χ^2_{21}

$$\frac{-\omega_{\text{bias}}(0)}{\omega_{z_{\text{exact}}}(0)} = 0.8185\left(\frac{\Delta}{L}\right)^{1.96} \tag{66}$$

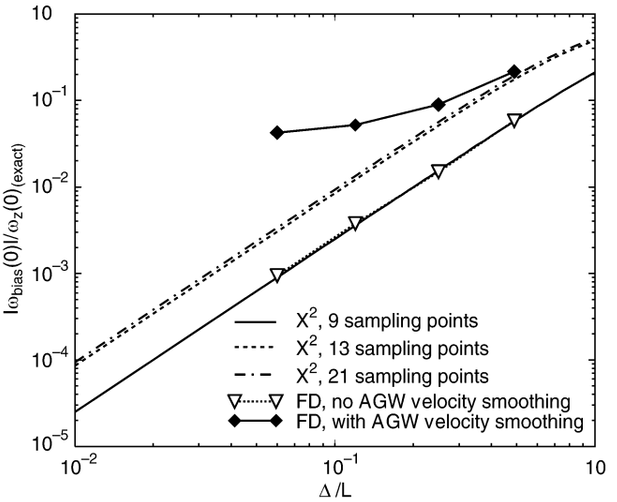

Fig. 5. Bias error at the vortex centre, i.e. $|\omega_{\text{bias}}(0)|/\omega_z(0)_{\text{exact}}$ as a function of normalised velocity sampling distance Δ/L for the χ^2 vorticity calculation method when 9, 13 and 21 velocity sampling points are used in the interpolation process and for the FD and AGW-FD vorticity calculation methods

The bias error introduced by the FD vorticity calculation method is identical to that introduced by the χ^2_9 method as shown in Fig. 5. The maximum bias error versus Δ/L relationship for the AGW-FD vorticity calculation method does not follow the approximate quadratic power law, but as shown in Fig. 5, it asymptotes towards the χ^2_{21} relationship with increasing Δ/L.

4.2 Effect of velocity random error

The following set of results from the numerical experiments relate to radial ω_z distribution measurements of the Oseen vortex based on discretised velocity field data which is generated using the exact velocity values of the Oseen flow field with superimposed Gaussian noise of a given standard deviation, σ_u. The noisy velocity field data for the numerical experiments was calculated as follows: (i) at each r/L value a spatially discretised exact local velocity field is established in the neighbourhood of the r/L point with the sampling velocity points positioned on a regular grid as shown in Fig. 1; (ii) zero mean Gaussian noise with a chosen standard deviation of σ_u px/s is then added to each velocity component prior to vorticity calculation. One hundred Angular positions for a given r/L are randomly chosen and 1000 samples of the vorticity are calculated for each angular position, providing a sample space of 10000 for each r/L. The mean error and standard deviation of ω_z, i.e. ω_{bias} and $\sigma(\omega_z)$ respectively, are then computed for each r/L station. The statistics were checked for convergence and it was found that convergence was usually achieved with 1000 samples. In addition the overall standard deviation and zero-mean probability distribution function (PDF) covering all vorticity data for all r/L stations was computed. The latter showed that ω_z' has a Gaussian PDF and that

$$\frac{\sigma(\omega_z,\ r/L)}{\sigma(\omega_z)} \approx 1$$

for all r/L, where $\sigma(\omega_z, r/L)$ denotes the standard deviation of ω_z at station r/L and $\sigma(\omega_z)$ denotes the standard deviation of all samples for one numerical experiment.

Figure 6 shows the effect of the velocity random measurement error on the vorticity measurement for the case where the velocity sampling points are separated by $\Delta/L = 0.25$ and 0.49. The effects of the random velocity measurement error are indicated by error bars which denote the magnitude of $\pm\sigma(\omega_z, r/L)$. The curve joining the centre of the error bars corresponds to the expected value of the measured vorticity minus the exact known vorticity normalised by the peak vorticity at $r=0$. According to Eq. (6) this difference is equal to ω_{bias}, i.e.

$$\omega_{\text{bias}} = E[\omega_z(r/L)] - \omega_{z_{\text{exact}}}(r/L).$$

Figure 6a and b correspond to the vorticity calculated using the AGW-FD method which is included for comparison. The bias error computed using the noisy velocity data is in good agreement with the bias error of the noise-free results for the AGW-FD method over the entire r/L range. In the case of the χ^2_{13} vorticity calculation method (Fig. 6c and d), the correspondence of the normalised ω_{bias} for noisy and noise-free velocity data exists only for $r/L \geqslant 1.5$. When $r/L > 1.5$, ω_{bias} for the noisy velocity deviates from the noise-free velocity data. The deviation is not large and not noticeable in a graph of the $\omega_z/\omega_{z_{\text{exact}}}(0)$ distribution. Nevertheless, it results in an overestimation of $E[\omega_z(r/L)]$ for $r/L > 1.5$ reaching a maximum at $r/L \approx 2.2$. The maximum location appears to be independent of the noise level in the velocity. For $r/L > 2.2$ the noisy vorticity bias error is found to relax back towards the noise-free bias error.

The results in Fig. 6a and c pertain to Gaussian velocity noise with $\sigma_u/V_{\text{ref}} = 0.018$, where V_{ref} is taken here as the maximum velocity of the Oseen vortex velocity field and the results in Fig. 6b and d pertain to Gaussian velocity noise with

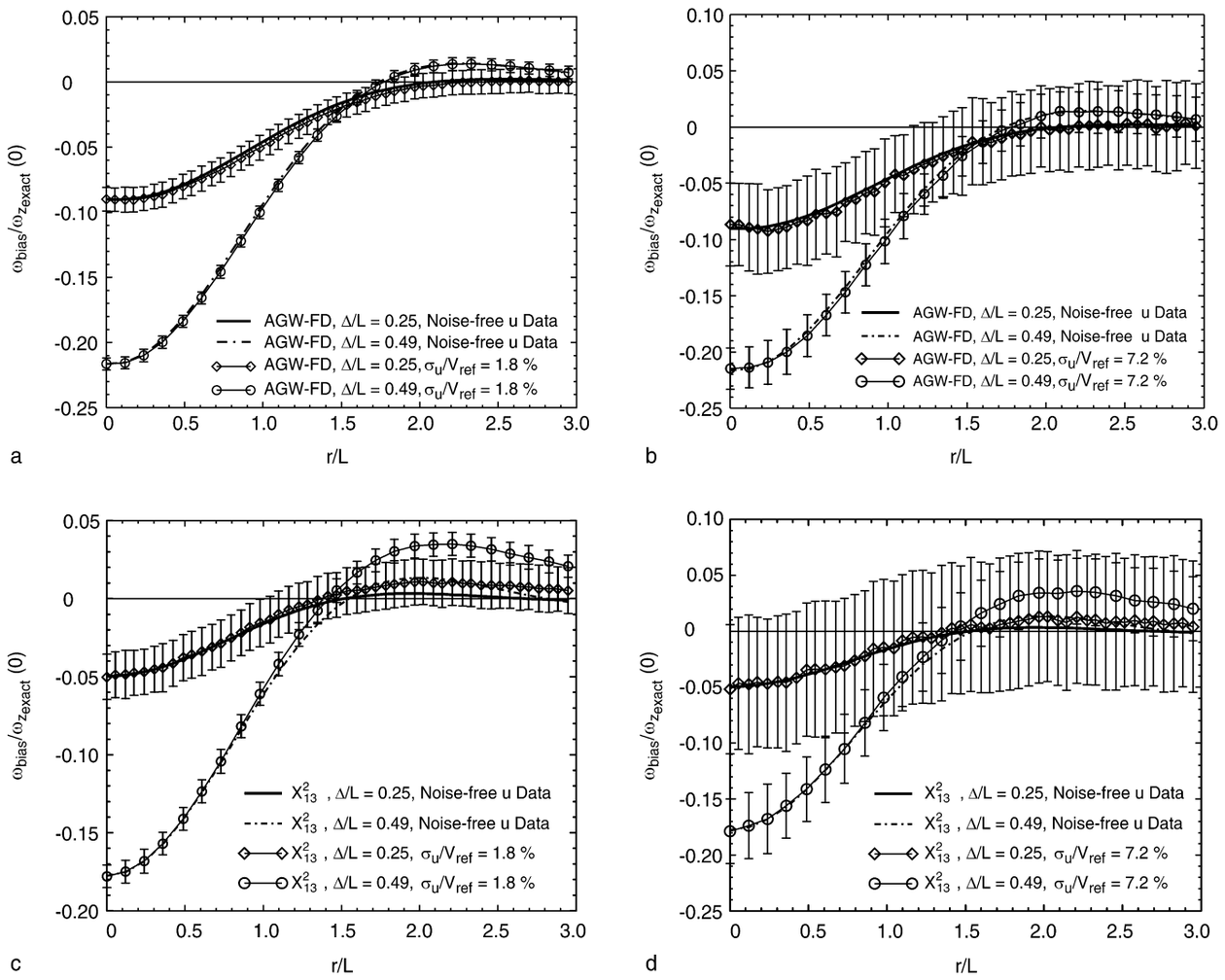

Fig. 6. Normalised bias and random error in ω_z computed from discretised velocity data consisting of the exact velocity field with superimposed Gaussian noise with a normalised standard deviation of $\sigma_u/V_{\text{ref}} = 1.8\%$ ((**a**) and (**c**)) and $\sigma_u/V_{\text{ref}} = 7.2\%$ ((**b**) and (**d**)). The error bars denote the normalised standard deviation of ω_z, i.e. $\sigma(\omega_z)/\omega_{z_{\text{exact}}}(0)$. The results in (**a**) and (**b**) correspond to vorticity calculations using the AGW-FD method, while (**c**) and (**d**) are the results for the χ^2_{13} method. Results for two velocity spatial sampling separations are presented, i.e. $\Delta/L = 0.25$ and 0.49

$\sigma_u / V_{ref} = 0.072$. The effect of increasing random error in the velocity measurement results, as expected, in increased scatter of the vorticity measurements relative to that determined using exactly known noise-free velocity data. This increase in scatter is manifested by the larger error bars, indicating a larger normalised $\sigma(\omega_z)$.

The corresponding results for the χ^2_{21} vorticity calculation method are similar to those presented in Fig. 6c and d with the bias error distribution nearly identical but with the random error reduced by 36%. These results tend to suggest that the χ^2_{21} vorticity calculation method is the optimum vorticity calculation method which, as shown in Fig. 5, has a bias error similar to the χ^2_{13} method, but has a smaller bias error compared to that of the AGW-FD method. At the same time the χ^2_{21} vorticity calculation method has a random error similar of the AGW-FD method which is smaller compared to the χ^2_{13} method.

Subtracting the appropriate bias error from the ω_z data permits the analysis of the distribution of the random ω_z error. This analysis shows that the normalised PDF of the random vorticity error resulting from velocity data with Gaussian noise with different standard deviation values all collapse onto the same Gaussian PDF.

As outlined in the theoretical analysis of the random vorticity error, λ_0 represents the ratio of the non-dimensional standard deviation of the vorticity to the non-dimensional standard deviation of the velocity. This value can be computed *a priori* without reference to any specific flow field. A number of numerical experiments, as outlined above, were conducted using noisy Oseen vortex flow fields with $\sigma_u / V_{ref} = 1.8\%$, 3.6% and 7.2% and covering a range of Δ/L values. Then λ_0 was calculated using the given value of σ_u and the estimated value of $\sigma(\omega_z)$. The latter was derived from the statistical analysis of the output of the vorticity calculation for the different vorticity calculation methods, i.e. χ^2_9, χ^2_{13}, χ^2_{21}, FD and the AGW-FD vorticity calculation method. The results of these numerical experiments are the symbols in Fig. 3. There is excellent agreement between the values of λ_0 derived from the statistical analysis of the numerical experiments and the *a priori* theoretical predictions of λ_0.

4.3 Discussion of bias and random vorticity error

The results presented in the previous section provide supporting evidence that the random error associated with the measurement of ω_z can be estimated using the theoretical results derived in Sects. 2 and 3.1. This prediction is in the first instance in the form of the non-dimensional ratio λ_0. The estimation of the dimensional $\sigma(\omega_z)$ requires the specification of a characteristic length scale and and estimation of σ_u, the measure of the velocity measurement random error. The acceptable level of random ω_z uncertainty depends on the significance to be associated with this measurement (Moffat 1988), e.g. a random uncertainty in ω_z of $\pm\sigma(\omega_z)$ implies a level of significance of 31.7%, whereas a random uncertainty in ω_z of $\pm 2.0\,\sigma(\omega_z)$ implies a level of significance of 4.6% and a random uncertainty in ω_z of $\pm 3.0\,\sigma(\omega_z)$ implies a level of significance of 0.3%.

The data in Fig. 3 clearly indicates that it is possible to have values of $\lambda_0 \leqslant 1.0$ depending on the vorticity calculation method and the normalised spatial velocity sampling separation. This is an interesting result, implying that for certain Δ/L values, the non-dimensional standard deviation (hence the random error) in the vorticity can be less than the non-dimensional velocity standard deviation. The results in Fig. 3 indicate that $\lambda_0 \leqslant 1.0$ is possible for the following vorticity calculation methods: χ^2_{13}, if $\Delta/L > 0.50$; χ^2_{21}; if $\Delta/L > 0.33$; AGW-FD, if $\Delta/L > 0.28$. For both the equivalent χ^2_9 and FD vorticity calculation methods $\lambda_0 \leqslant 1.0$ is only possible for $\Delta/L > 1$, which is an impractical case. Thus, the χ^2_{21} AGW-FD vorticity calculation methods imposes the least stringent restrictions on the spatial velocity sampling separation to minimise the transmission of the random velocity error into random vorticity error. However, this comes at the cost of a large bias error in the peak vorticity. Therefore, the use of either method with $\Delta/L \geqslant 0.5$ produces a maximum bias error at the peak vorticity point, which as indicated by the results shown in Fig. 5, can be larger than 22%. A slightly smaller value of $\Delta/L \approx 0.33$ using the χ^2_{21} vorticity calculation method results in $\lambda_0 = 0.99$ and a maximum bias error of 9.7% at the peak vorticity location.

These results clearly demonstrate that for all vorticity calculation methods presented in this paper, there are two opposing errors with Δ/L dependence. The larger the value of Δ/L (i.e. low spatial resolution velocity samples) the lower the random vorticity error in ω_z, but the higher the bias error in ω_z at the peak vorticity location, and conversely, the smaller the value of Δ/L (i.e. high spatial resolution velocity samples) the higher the random vorticity error in ω_z, but the lower the bias error in ω_z at the peak vorticity location. This result is graphically illustrated in Fig. 7. From the numerical experiments, the λ_0 values as predicted by the theoretical analysis are found to be independent of the σ_u value in the noisy discretised velocity data and independent of the spatial location.

This result is not surprising as larger velocity sampling separations tend to smear (smooth) spatial variations and

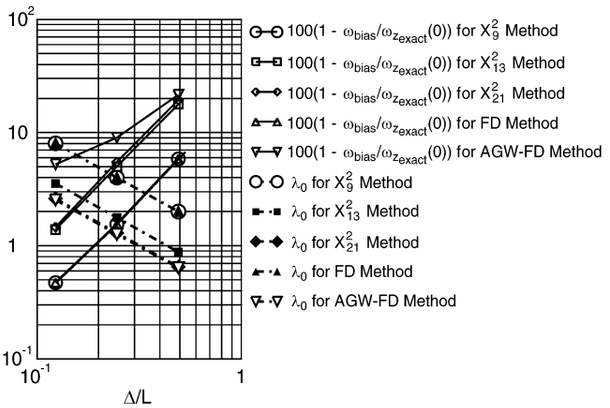

Fig. 7. Bias error and λ_0 variation with Δ/L for the Oseen vortex flow at $r = 0$. The data was determined from noisy discretised velocity samples using all the vorticity calculation methods described in this paper. The sample space for the statistical analysis of each data point is 10000

hence, random error due to a lack of spatial resolution, i.e. thus acting like a low-pass filter. This explains the underestimation of vorticity peaks. In contrast, high velocity spatial resolution faithfully represent velocity variations, and hence, tends to allow random velocity errors to pass through the vorticity calculation method unattenuated, resulting in noisier vorticity measurements but also less attenuation of vorticity peaks.

4.4
DPIV experiments with computer generated images

Digital image frames of seed particle motion subjected to the Oseen vortex flow were generated on a frame of size 780×780 px. The particles were distributed randomly in the first digital frame. The images of the particles have a Gaussian intensity distribution with a diameter of 1.5 ± 0.5 px. Subsequent digital frames are generated by advancing the centres of the particle images in time using the Oseen vortex velocity field and a 5th order Runge–Kutta integration scheme with 100 time steps over the time step Δt, which represents the time interval between the acquisition of two frames in an experiment. The new frame is then generated using the stored size characteristic of each particle and its new position. All digital frames have an 8 bit dynamic intensity range to be consistent with the dynamic range which is available on most commonly available digital cameras.

A sequence of 200 digital images equally separated in time by a uniform Δt was generated using the method just outlined. The entire set of computer generated digital PIV images was analysed using CCDPIV with sub-pixel resolution (Soria 1996). The sampling window size of 32 px $\times$ 32 px was used to analyse these images. The resulting normalised velocity sampling distance is $\Delta / L = 0.25$. Figure 8 shows the compilation of the velocity measurements from the 200 images as a function of normalised radius from the vortex core. At each r/L station the mean tangential velocity agrees very well with the exact velocity as shown in Fig. 8a. The variation of the DPIV measurement of u_t, the tangential velocity, at each r/L is given by the error bars which represent $\pm \sigma(u_t)$. The maximum variation in the u_t measurements is found to occur near the maximum tangential velocity. The standard deviation of the error in u_t for all the samples is found to be approximately 0.027 px/s. Figure 8b shows u_r, the radial velocity. The mean measurement of the radial velocity is also found to agree very well with the exact zero radial velocity of the Oseen vortex flow. The variation in these measurements is again represented by the vertical error bars which show the corresponding $\pm \sigma(u_r)$ variation of these measurements. The maximum local variation in these measurements is also found to correspond with the region around the maximum tangential velocity. The standard deviation of the error in u_r is found to be 0.023 px/s. The standard deviations of the error in the horizontal and vertical component measurements are found to be approximately equal and have a value of $\sigma(u) \approx \sigma(v) \approx 0.025$ px/s. These results provide support for the assumption of equal standard deviation values for the horizontal and vertical velocity component measurements made in the analysis in Sect. 3.1.

The out-of-plane vorticity was calculated from the in-plane CCDPIV velocity measurements using the χ^2_{13} and χ^2_{21} vorticity calculation methods. The solid line in Fig. 9a and b represents the ω_z derived from exact velocity data at the CCDPIV velocity

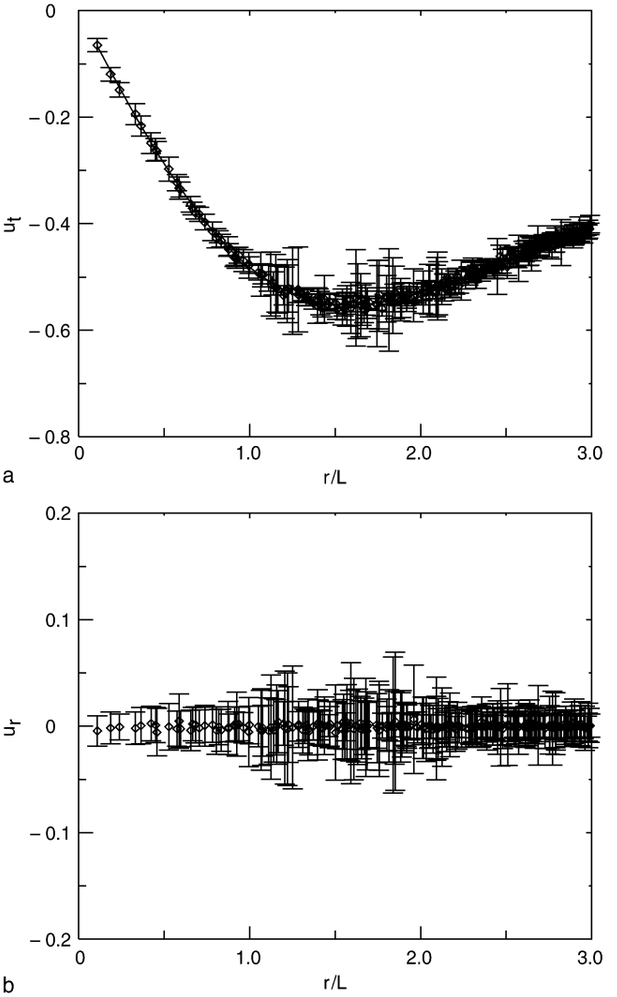

Fig. 8a,b. The Ossen vortex velocity distribution determined using CCDPIV of computer generated digital images. **a** Tangential velocity u_t, **b** radial velocity u_r. The solid line in (**a**) is the exact Oseen vortex tangential velocity while the diamonds correspond to mean DPIV measurement. The error bars indicate one standard deviation of the respective CCDPIV samples

sample points, whereas the symbols represent the mean vorticity measurement at each r/L derived from the 200 CCDPIV velocity fields. The vertical error bars show the variation of the vorticity measurements based on a minimum of 200 samples and represent $\pm \sigma(\omega_z)$ for each r/L. This variation is reasonably uniform throughout the domain except at $r/L \approx 3$, where the variation is found to be somewhat larger due to frame edge effects.

As expected the variation of ω_z is found to be smaller for the χ^2_{21} vorticity calculation method compared to the χ^2_{13}.

The standard deviation of the random error in ω_z for the entire data base shows that using: (i) the χ^2_{13} vorticity calculation method results in $\sigma(\omega_z) = 0.00033$ s^{-1} and (ii) the χ^2_{21} vorticity calculation method results in $\sigma(\omega_z) = 0.00026$ s^{-1}. These values for $\sigma(\omega_z)$ in conjunction with the value of $\omega_u = 0.025$ px/s and the characteristic length scale L = 130 px allows the calculation of the corresponding λ_0 values. Thus, the

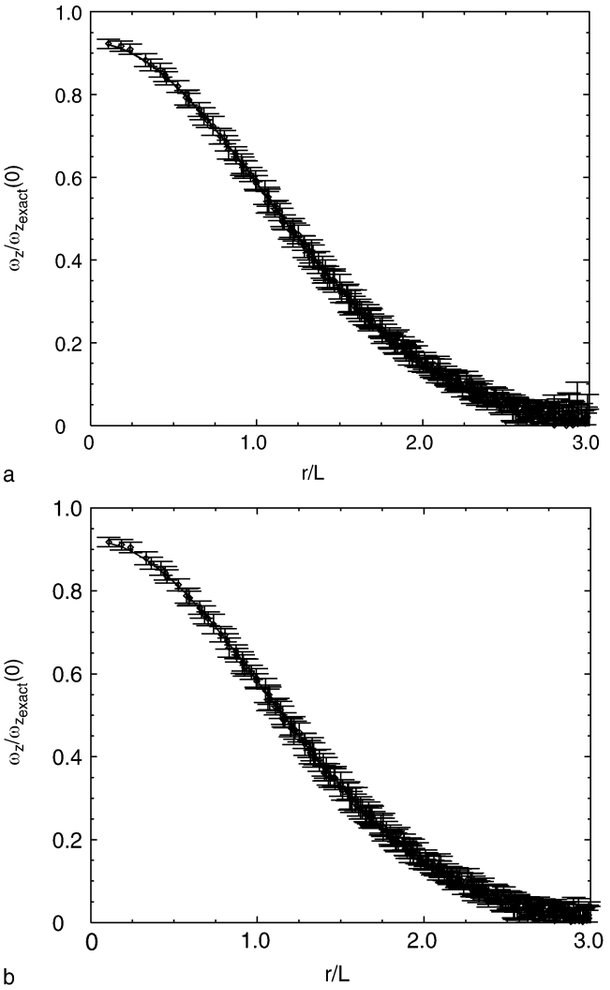

Fig. 9a, b. The Oseen vortex vorticity distribution determined using CCDPIV velocity data (see Fig. 8) from computer generated digital images. The velocity sampling separation is $\Delta/L=0.25$. ω_z computed using. **a** The χ^2_{13} vorticity calculation method, **b** the χ^2_{21} vorticity calculation method. The solid line corresponds to ω_z determined from the exact Oseen vortex velocity field samples at the same positions as the CCDPIV data while the diamonds correspond to mean ω_z determined from the CCDPIV velocity mesurement. The error bars indicate one standard deviation of the respective ω_z samples

χ^2_{13} vorticity calculation method results in $\lambda_0=1.70$, which compares favourably with an *a priori* predicted value of 1.77 using Eq. (54). Similarly, for the χ^2_{21} vorticity calculation methods, it is found that $\lambda_0=1.34$, which is in excellent agreement with the *a priori* prediction of $\lambda_0=1.34$ using Eq. (55).

Therefore, as predicted from the theoretical analysis of the random vorticity error, an increase in the number of data points used in the χ^2 vorticity calculation method reduces the random error. However, this comes at the expense of an increased underestimation of the peak vorticity, identified as an increased bias error. This is evident when comparing the ω_z data shown in Fig. 9a resulting from the χ^2_{13} vorticity calculation method with that shown in Fig. 9b resulting from the χ^2_{21} vorticity calculation method. The bias error is larger in the results shown in Fig. 9b than in a, although the difference is small for these data sets. This result is consistent with that presented in Fig. 5. Thus, as discussed in Sect. 4.3, for a given velocity data spatial sampling separation and a fixed random velocity measurement error, a reduction of random ω_z error and a simultaneous reduction in bias error of the peak vorticity cannot be accomplished. In summary, a reduction of the random error by using more data points increases the bias error and visa versa.

5
DPIV application: a Laminar vortex ring experiment

In this section the application of the vorticity error analysis is illustrated on the out-of-plane vorticity field derived from in-plane velocity measurements. The in-plane velocity measurements were determined from CCDPIV analysis of digital images of a physical laminar vortex ring.

5.1
Experimental apparatus

The experiments were carried out using water in the apparatus depicted in Fig. 10. The vortex ring was generated by pushing a piston through a circular tube of 56.6 mm inner diameter. A 50 mm diameter orifice plate was positioned at the exit. The tube is connected to an enclosed perspex tank of internal dimensions 1100 mm × 500 mm × 500 mm. The tank was filled with water at a temperature 17.1 °C during the experiment. The driving mechanism for the piston is a computer controlled micro-step stepper motor with a directly coupled position encoder. This is connected to a precision 20 mm diameter ball screw with a 5 mm lead. The nut was bolted to a 20 mm diameter stainless steel push rod and a guide riding on a 20 mm diameter stainless steel guide rod for stability. A machined stainless steel piston with a PVC face was connected to the push rod.

The piston velocity for the experiments presented in this paper was 0.02 m/s (i.e. 4 rev/s) with a displacement resolution of 20 μm/step. The piston velocity is taken here as the characteristic velocity, V_{ref}. The stroke length used was equal to the orifice diameter, i.e. D = 50 mm. The total mechanical impulse was 0.0019635 kg m/s and the Reynolds number based on exit diameter (i.e. orifice diameter) and piston velocity was 933. The circulation for half of the vortex ring using the "slug-model" (Glezer and Coles 1990) was calculated as $\Gamma=0.0005$ m^2/s.

The water was seeded to a concentration of 0.011 kg/(m^3 of H_2O) with hollow glass micro spheres which have a mean diameter of 11 μm and a S.G. = 1.1. Two co-planar laser sheets in the x–y plane (see Fig. 10 for coordinate axis definition) were used to illuminate the seeding particles. The laser sheets were generated by two frequency doubled, 1 J Nd:YAG lasers producing 6 ns laser pulses with 400 mJ at 532 nm. The beams from these lasers were positionally combined using a polarising beam splitter plate and shaped into 1 mm thick laser sheets using appropriate spherical and cylindrical lenses.

Single exposed digital images of the seed particles were acquired using a Kodak Megaplus XHF digital camera with a 1000 px × 1000 px array and a maximum framing rate of 30 Hz. A 105 mm Micro-Nikkor lens set at $f\#=4$ was used to view the region of interest in the x–y plane. The Kodak

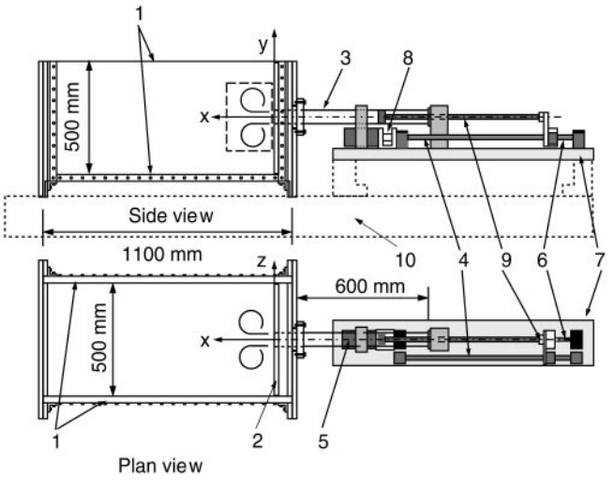

Fig. 10. Diagram of the vortex ring facility: 1. 25 mm thick perspex walls, floor and roof, 2. false 25 mm thick perspex wall, 3. 56.5 mm inner diameter perspex tube, 4. 20 mm diameter stainless steel guide rod, 5. micro-step computer controlled stepper motor with position encoder, 6. 20 mm diameter precision ball screw with 5 mm lead, 7. machined aluminium support and mounting plate, 8. direct drive coupling between stepper motor and ball screw, 9. 20 mm diameter stainless steel pushrod and piston with PVC piston face, 10. optical breadboard table. A 50 mm diameter orifice plate was mounted flush on the false perspex wall with its axis aligned colinear with the perspex tube axis

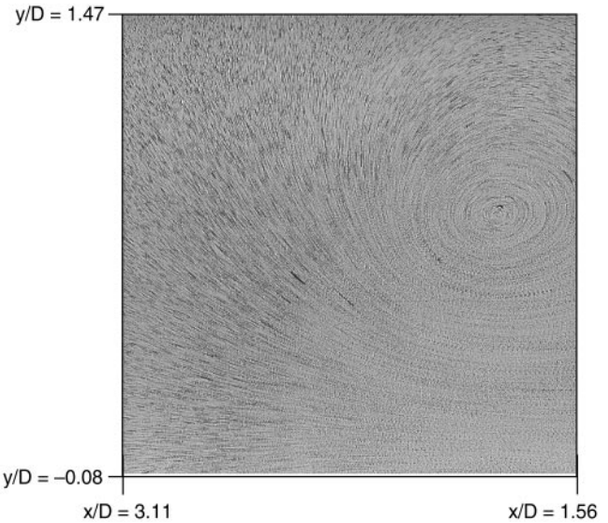

Fig. 11. Flow visualisation of half the vortex ring at $Re = 933$, achieved by summing 63 digitally acquired single-exposed images

Megaplus XHF digital camera was controlled using an Imaging Technology IC-PCI digital frame grabber installed in a Pentium based PC equipped with 64 MB of RAM, allowing digital image acquisition at 22 Hz framing rate directly into the PC RAM. For the present experiments the time between the frame acquisitions was set to 50 ms. Digital pairs of images were analysed using the in-house developed, parallelised, multi-processor version of the CCDPIV analysis program "CCPIV" (Soria 1996) on a SGI Power Challenge computer equipped with $12 \times$ MIPS R10000 CPUs and 2 GB of RAM.

5.2 Experimental in-plane velocity and out-of-plane vorticity results

Figure 11 shows a digital superposition of several images of half the vortex ring, flow is from right to left. Pairs of these individual images were used in the CCDPIV analysis. Square interrogation windows of two sizes (SWS) were used. The digital images were analysed using a number of velocity sampling separations for the SWS = 32 px case, i.e. $\Delta/\mathrm{SWS} = 1.0$, $\Delta/\mathrm{SWS} = 1.5$, $\Delta/\mathrm{SWS} = 2.0$ and $\Delta/\mathrm{SWS} = 3.0$. The images were also analysed using SWS = 64 px and with $\Delta/\mathrm{SWS} = 1.0$

In none of the cases presented was overlap CCDPIV processing used. Figure 12 shows the results of each CCDPIV analysis for the same pair of digital images of the 63 image set. The vortex ring moves from top to bottom in these plots with the left bottom corner, which is identified as the origin in these plots, corresponding to $x/D = 3.11$ and $y/D = 1.47$ in the xyz coordinates shown in Figs. 10 and 11. The convection velocity of the peak vorticity point for the case corresponding to Fig. 12a has been removed from all the velocity fields shown in Fig. 12. In addition the velocity has been normalised by the piston velocity, i.e. V_{ref}.

During the CCDPIV analysis only data with a normalised cross-correlation peak greater than 0.9 and with a displacement less than or equal to $(0.3 \times \mathrm{SWS})$ was accepted as a valid measurement. The CCDPIV analysis produced 100% valid measurements with these conditions. Following the CCDPIV analysis of all 63 image pairs with the set SWS and Δ/SWS values, the uncertainty in the CCDPIV velocity measurement, i.e. $\sigma_{\delta u}$, was computed for that data set using the procedure outlined in Sect. 3.1. The appropriate equation chosen from Eqs. (58)–(60) was then used to calculate the corrected random error in the CCDPIV measurements, i.e. $\sigma_u/V_{\mathrm{ref}}$. For the SWS = 32 px analysed data the corrected random error in the velocity was found to be $\sigma_u/V_{\mathrm{ref}} \approx 2.3\%$, whereas for the SWS = 64 px analysed data the corrected random error in the velocity was found to be $\sigma_u/V_{\mathrm{ref}} \approx 1.6\%$

The value of $\sigma_{\delta u}$ was also employed as a post-processing tool to reject "bad" CCDPIV data. The following algorithm was employed for this procedure: if the CCDPIV measurement deviated by more than $\pm 2\sigma_{\delta u}$ from the local χ^2_{13} *velocity* fit, then that CCDPIV velocity measurement was rejected and replaced by the local χ^2_{13} *velocity* fit at that point. This procedure resulted in rejection of at most 5% of the CCDPIV measurement in one image pair, with most rejection levels per image pair lying between 0–2%.

An immediate observation from the velocity maps presented in Fig. 12 is that a lack of velocity sampling resolution results in the misinterpretation of the in-plane vortex ring geometry. In the lowest sampling resolution data shown in Fig. 12d the vortex ring flow looks approximately axisymmetric, whereas the CCDPIV measurements with higher velocity sampling resolution shown in Fig. 12a and b clearly show that the vortex ring flow is not axisymmetric but is stretched in the vortex ring

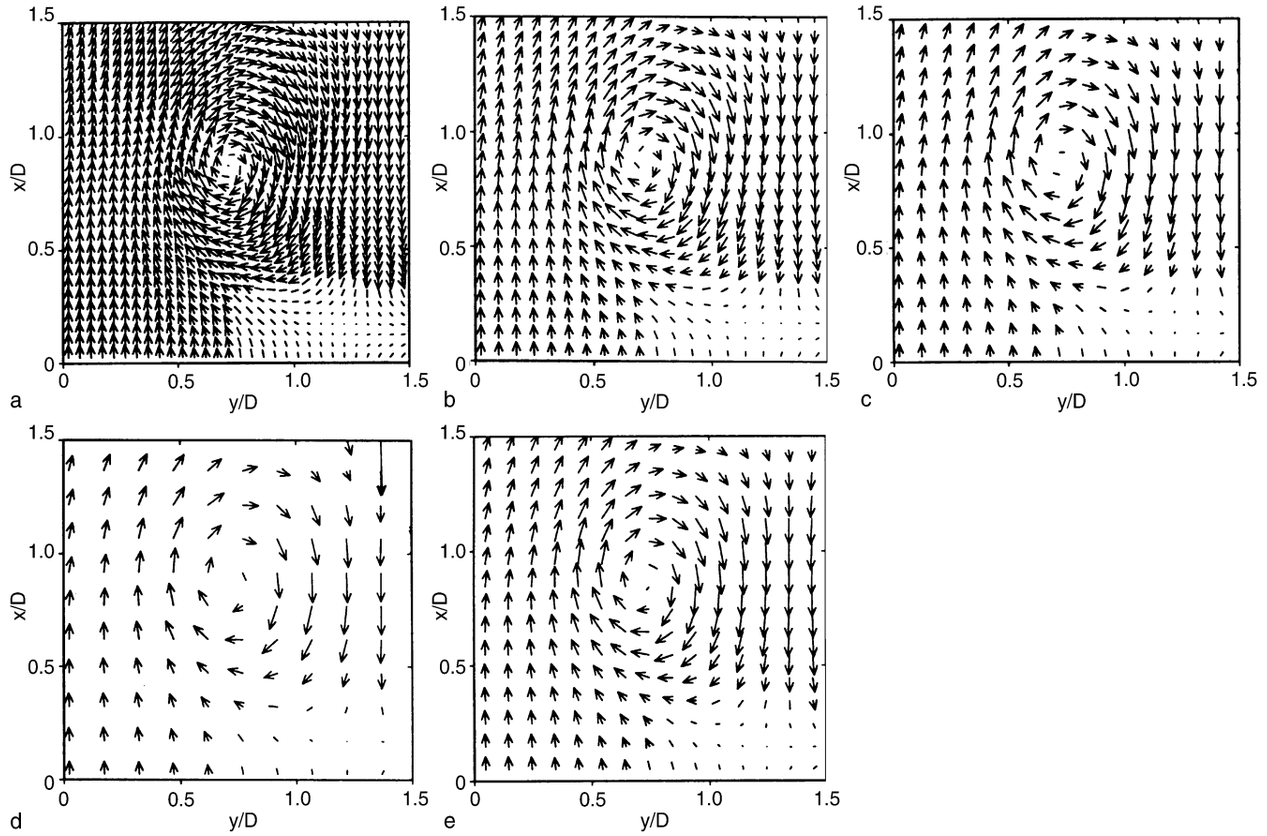

Fig. 12a–e. CCDPIV measured velocity field using an interrogation window of size SWS = 32 px. in (**a**)–(**d**) and SWS = 64 px in (**e**). The velocity sampling separations are. **a** $\Delta/\mathrm{SWS}=1.0$, **b** $\Delta/\mathrm{SWS}=1.5$, **c** $\Delta/\mathrm{SWS}=2.0$, **d** $\Delta/\mathrm{SWS}=3.0$, **e** $\Delta/\mathrm{SWS}=1.0$. The convection velocity at the location of peak vorticity, i.e. $x_0/D=0.87$ and $y_0/D=0.72$ as determined from the analysed data in (**a**) has been subtracted from all velocity fields. The velocity is non-dimensionalised with the piston velocity and the vectors are scaled with a factor of 0.25

propagation direction and contracted normal to this propagation direction. This result is also confirmed in the corresponding out-of-plane vorticity maps computed using the χ^2_{13} vorticity calculation method shown in Fig. 13. The lowest spatial resolution case (Fig. 13d) is approximating an axisymmetric vorticity distribution shape, whereas the highest spatial resolution case (Fig. 13a) shows that the vorticity distribution is more elliptical with the major axis in the propagation direction of the vortex ring. The vorticity in the vorticity maps shown in Fig. 13 are normalised by the ratio of the piston velocity to orifice diameter and all are plotted using the same contour levels.

Figures 13a–d clearly show the bias effect of increasing underestimation of the peak vorticity with lowering velocity spatial sampling resolution. In the $\Delta/\mathrm{SWS}=1.0$ case the largest negative vorticity contour level plotted corresponds to $\omega_z D/V_{\mathrm{ref}}=-5$, whereas in the $\Delta/\mathrm{SWS}=3.0$ case the largest negative vorticity contour level plotted is $\omega_z D/V_{\mathrm{ref}}=-2.5$. In other words, there is an underestimation of the vorticity of up to 50% in the vortex core region in the lowest spatial resolution velocity measurements relative to the highest spatial resolution velocity measurements.

The random error in ω_z was estimated using the procedure outlined at the end of sect. 3.1, resulting in the following estimates for the normalised standard deviations in the ω_z measurements: the data in Fig. 13a has $\sigma(\omega_z)\,D/V_{\mathrm{ref}}=0.2$; the data in Fig. 13b has $\sigma(\omega_z)\,D/V_{\mathrm{ref}}=0.15$; the data in Fig. 13c has $\sigma(\omega_z)D/V_{\mathrm{ref}}=0.1$; and the data in Fig. 13d has $\sigma(\omega_z)D/V_{\mathrm{ref}}=0.07$ and the data in Fig. 13e has $\sigma(\omega_z)D/V_{\mathrm{ref}}=0.05$. The uncertainty in the ω_z measurements depends on the confidence level assigned to these measurements. The decrease in the ω_z random error with decreasing velocity spatial sampling resolution predicted using the analytical results developed in this paper are also qualitatively illustrated in the vorticity maps shown in Fig. 13. The vorticity maps derived from the lower spatial sampling resolution CCDPIV measurements are considerably smoother than those derived from the higher spatial sampling resolution CCDPIV measurements. The estimated uncertainty in the CCDPIV velocity measurements in both these cases are approximately equal.

The peak vorticity location was determined to be at $x_0/D=0.87$ and $y_0/D=0.72$ using the CCDPIV data analysed with SWS = 32 px and $\Delta/\mathrm{SWS}=1$. The circulation around this peak vorticity location was computed using the velocity line integral,

$$\Gamma_{L_I}=\int_{C_{L_I}}\mathbf{u}\cdot\mathrm{d}\mathbf{l} \tag{67}$$

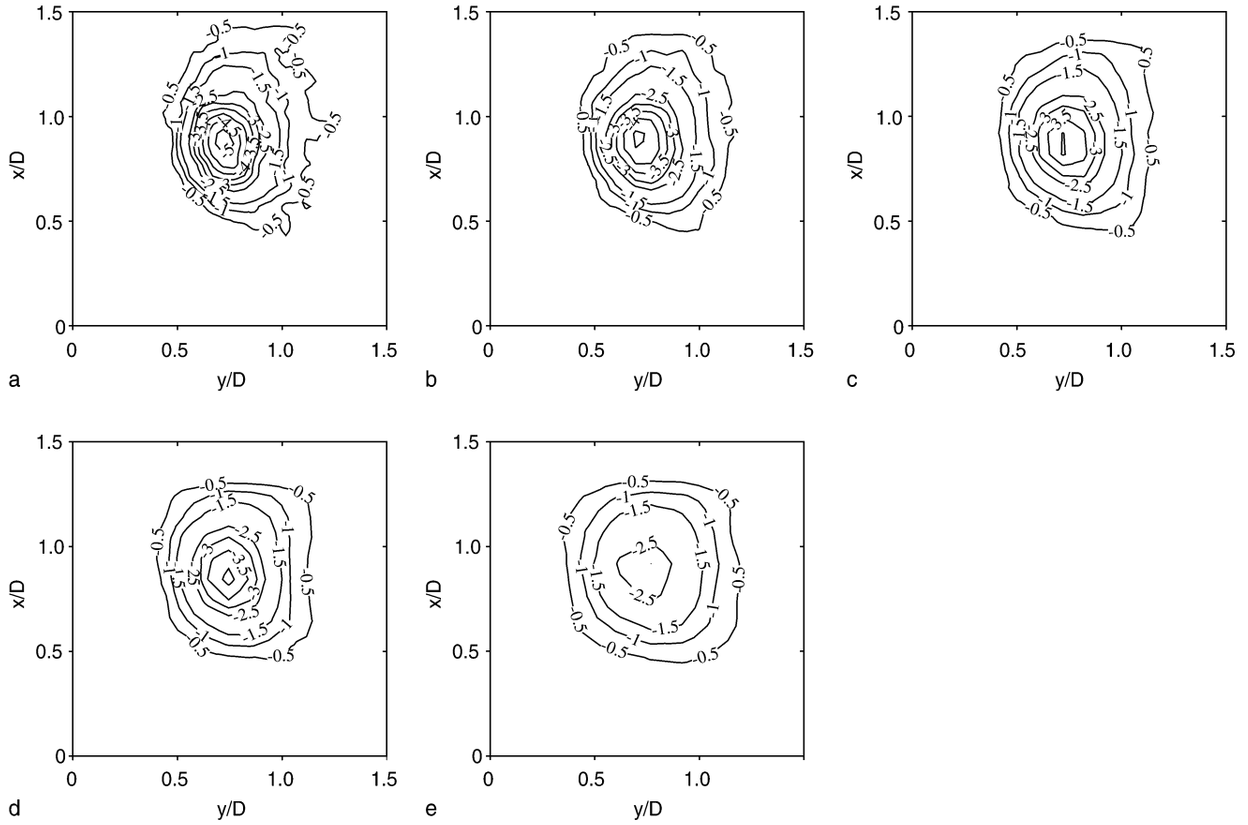

Fig. 13a–e. The normalised vorticity corresponding to the velocity fields shown in Fig. 12. The vorticity is normalised with the ratio of the piston velocity to the orifice diameter, D

and the vorticity surface integral,

$$\Gamma_{L_I} = \int_{L_I \times L_I} \boldsymbol{\omega} \cdot \mathrm{d}\mathbf{A} \tag{68}$$

The L_I subscript is used to identify that the circulation is taken over a square area with sides of length L_I. C_{L_I} identifies the circuit enclosed by the square box and d**A** is the infinitesimal area dA with outward pointing unit normal **n**, i.e. d**A** = **n** dA. Both these integrals were computed numerically using the extended trapezoidal rule. The integrand was computed using local χ^2_{13} velocity interpolation in the numerical computation of Eq. (67) and the χ^2_{13} vorticity calculation method was employed in the numerical computation of Eq. (68). The Γ_I integrals were deemed to have converged when the relative change in the integral between 2 stages did not vary by more than 10^{-2}. The circulation calculation shows another attractive feature of local χ^2 fitting, namely, that the velocity can be interpolated readily at any point within the domain of the fit, and equivalently, that the vorticity is immediately available at any point within the local domain of the velocity fit.

The results of the circulation calculations are presented in Fig. 14. Unless otherwise stated in this graph all the velocity measurements relate to CCDPIV analysis with SWS = 32 px. Γ_{L_I} for all cases is normalised by the maximum circulation computed from the highest resolved CCDPIV velocity measurements (i.e. SWS = 32 px, Δ/SWS = 1). The results in this graph show that the vorticity integral method slightly underestimates Γ_{L_I} relative to the velocity integral method for $L_I/D \leqslant 0.2$. This underestimation can be explained by the smoothing introduced into the vorticity using the χ^2_{13} vorticity calculation method that is manifested more significantly near the peak vorticity region and hence, it is only reflected in Γ_I near the vortex core. The lower velocity sampling resolution data underestimates Γ_I over most of the L_I/D domain. Although it is observed that all CCDPIV data sets approach the same maximum circulation at $L_I/D = 1$, the convergence towards this maximum circulation for the CCDPIV data analysed using SWS = 32 px with Δ/SWS = 3 is very slow. The results in Fig. 14 provide further evidence of the biasing underestimation of the peak vorticity, here in the form of Γ_{L_I}. This effect is even observed in the circulation calculated using the velocity integration method in some of the cases shown in Fig. 14 due to low spatial sampling resolution of the velocity.

The value of $\Gamma_{\max}$ based on the circulation calculation outlined above with the "best" estimate for $\omega_{\max}$ can be used to estimate a value for L based on the maximum vorticity formula of the Oseen vortex vorticity distribution, i.e.

$$L = \sqrt{\frac{-\Gamma}{2\pi\omega_z(0)}} \tag{69}$$

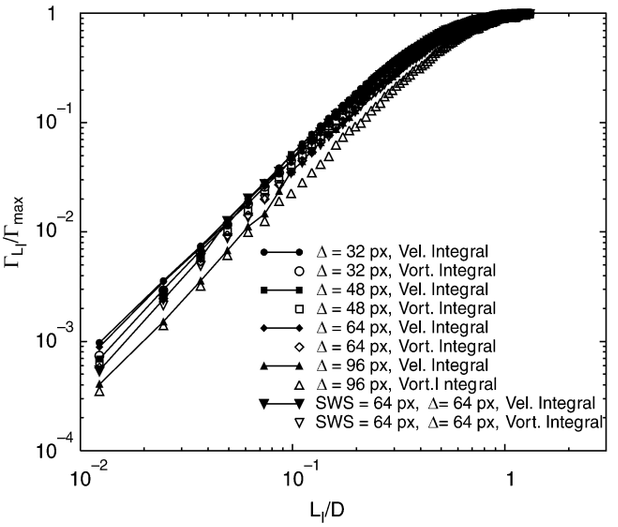

Fig. 14. Normalised circulation as a function of the normalised square integration box size, L_I/D, where D is the orifice diameter of the vortex ring apparatus. The circulation was computed: (i) using the velocity line integral identified on the plot as "*Vel. Integral*" using the CCDPIV velocity data, and (ii) using the vorticity surface integral identified on the plot as "*Vort. Integral*" using the vorticity calculated from the CCDPIV velocity data using the χ^2_{13} vorticity calculation method. Unless otherwise stated the DPIV velocity was derived using interrogation windows of size SWS = 32 px. Data for different velocity sampling separations, Δ, are presented

Substituting Γ_{max} for $-\Gamma$ and ω_{max} for $\omega_z(0)$ in this equations results in $L = 115.7$ px. The "best" estimate of the peak vorticity and its location was determined from the CCDPIV data analysed using SWS = 32 px with $\Delta/\mathrm{SWS} = 1$ using the following procedure. Following the calculation of ω_z using the χ^2_{13} vorticity calculation method, the peak vorticity and its location is found using a linear search. A local two-dimensional Gaussian least square fit is then employed to determine the peak vorticity and its location more precisely.

Figure 15 displays the normalised vorticity distributions in the two orthogonal directions passing through the point of peak vorticity found to be located at $x_0/D = 0.87$ and $y_0/D = 0.72$. The vorticity is normalised by the peak vorticity and the (x, y) coordinates have been appropriately shifted and then normalised with the estimated value of L. The error bars in the vorticity indicate the estimated values of $\sigma(\omega_z)/\omega_{max}$ determined using the procedure outlined at the end of Sect. 3.1. The corresponding normalised Oseen vortex vorticity distribution is also plotted for comparison. This data clearly shows that there is a large bias error introduced in ω_z measurement due to a lack of spatial velocity sampling resolution as predicted in the theoretical/numerical analysis presented in Sect. 4.1. This error, which is often not accounted for by many investigators presenting vorticity distributions, can readily result in vorticity errors of 30–50% or even larger, as shown in Fig. 15. The opposing effect of a decreasing random error with decreasing velocity sampling resolution is also demonstrated in Fig. 15 by the smaller error bars for the larger velocity sampling separation cases.

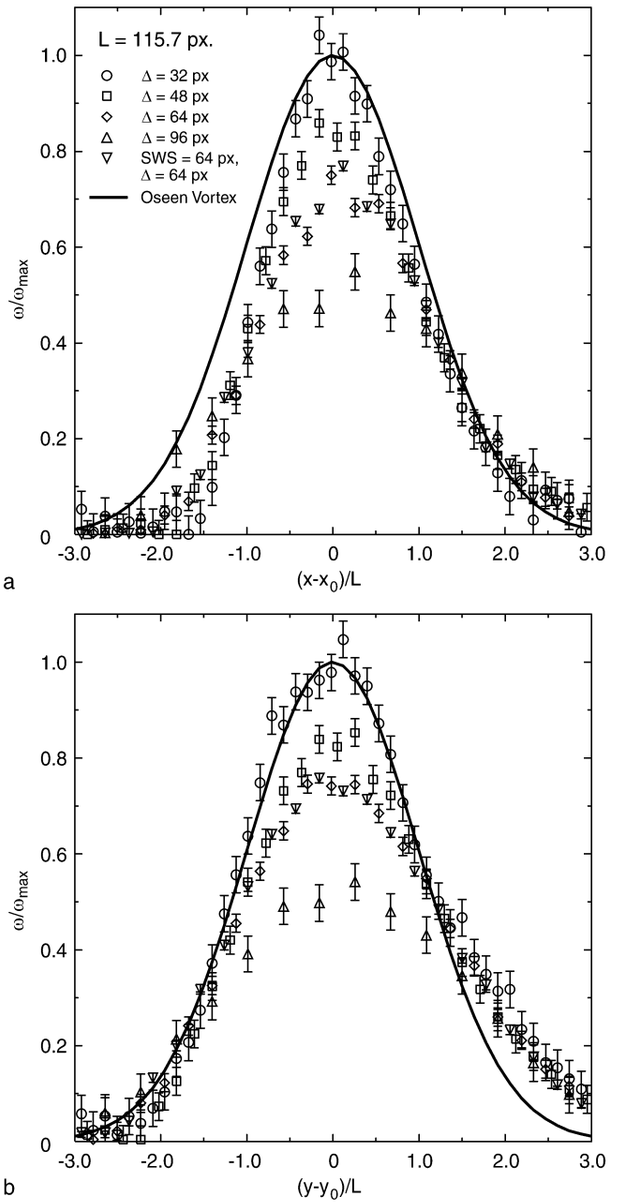

Fig. 15. Normalised vorticity distribution in the flow direction (**a**) and across the flow direction (**b**) at peak vorticity location, i.e. $x_0/D = 0.87$ and $y_0/D = 0.72$ as determined from the analysed data in Fig. 12a. The distributions for different velocity sampling separations and with SWS = 32 px are shown, in addition to the analysis case with SWS = 64 px and $\Delta/\mathrm{SWS} = 1.0$. The Oseen vortex vorticity distribution with $L = 115.7$ px estimated from the data in Fig. 12a is also shown for comparison. The error bars represent the estimated 1 standard deviation of the vorticity measurement

Comparing the data set analysed using SWS = 32 px with $\Delta/\mathrm{SWS} = 2$ with the data set analysed using SWS = 64 px with $\Delta/\mathrm{SWS} = 1$, one notes that the bias error is approximately equal in both cases. This is expected, as the bias error depends predominantly on the normalised velocity sampling separation, Δ/L, which is equal for both data sets. These physical

experimental results should be considered with the following point in mind, namely that each data point in Figs. 12, 13 and 15 now only represents a single sample. This is different to the data presented in the numerical experiments where a mean vorticity distribution was calculated from essentially equal experiments with Gaussian noise.

Comparing the random error in the vorticity computed from CCDPIV data analysed using SWS = 32 with Δ/SWS = 2 to the random error in the vorticity computed from CCDPIV data analysed using SES = 64 px with Δ/SWS = 1, it is found that the latter has a smaller random error. This is due to the smaller velocity error, σ_u, which in turn is a result of having more seed particles in the interrogation window available during the CCDPIV analysis. A greater numbers of seed particles reduces the uncertainty in the cross-correlation peak and its location. This reasoning presumes that the velocity gradients are still small within the larger interrogation window with SWS = 64 px. The larger window in general has the undesirable effect of smearing (smoothing) out velocity gradients across the interrogation window, resulting in CCDPIV measurements with a lower σ_u but increased filtering of velocity gradients.

The measurements presented in Fig. 15 show that the Oseen vortex vorticity distribution is a reasonably good model for the experimentally determined vorticity distribution near the vortex core of the vortex ring. In order to test the predictive equations for the bias error derived in Section 4.1. Eq. (65) which represents the bias vorticity error introduced by using the χ^2_{13} vorticity calculation method is plotted in Fig. 16. The corresponding experimentally determined bias error is also plotted. The error bars on the experimental data indicate the random error in terms of $\pm 1\sigma(\omega_z)/\omega_{\max}$. Even at this low confidence level of 68.3%, the predictive Eq. (65) based on the Oseen vortex for bias error estimation at the peak vorticity location appears to be a good model.

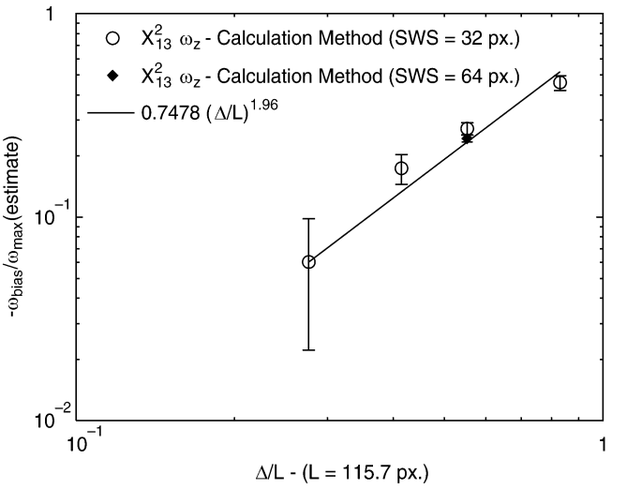

Fig. 16. Bias error in the peak vorticity, where the vorticity has been calculated using the χ^2_{13} vorticity calculation method. The error bars represent the estimated 1 standard deviation of the vorticity measurement. The solid line is the predictive curve for the underestimation of the peak vorticity for an axisymmetric Oseen vortex

6 Conclusions

This study has quantitatively shown the effects of velocity spatial sampling separation and random velocity measurement error on the accuracy of vorticity distribution measurements using: (i) the finite difference vorticity calculation method (FD), (ii) the adpative Gaussian window smoothing of the velocity field with finite difference vorticity calculation method (AGW-FD) and (iii) the local χ^2 velocity fit with analytic differentiation vorticity calculation method (χ^2_x). In all methods the effect of increasing velocity spatial sampling separation is to introduce a larger bias error, resulting in an increasing underestimation of the vorticity in the peak vorticity regions. The effect of the random velocity measurement error is to scatter the vorticity measurements around the corresponding biased vorticity. The bounds of vorticity scatter are dependent on the random error in the velocity measurements, (i.e. the standard deviation of the velocity, $\sigma(u)$) and the vorticity calculation method.

A general framework for the analysis of the transmission of the velocity random error into the vorticity random error has been developed in this paper. Analytically developed, non-dimensional transmission factors describing the transmission of the velocity random error into vorticity random error for the special case of velocity samples available on a structured rectangular grid with measurement error which is spatially homogeneous, isotropic and Gaussian, are presented in this paper. Numerical experiments using analytically known velocity fields with and without superimposed Gaussian noise have been used to provide supporting evidence confirming the applicability of the theoretical results for the random velocity error transmission.

It was found that the FD and χ^2_9 vorticity calculation methods are identical in all respects. The only benefit of using the latter is that it can immediately provide the vorticity, not only at the velocity sampling point, but also anywhere within the domain of the local χ^2 velocity fit.

The AGW-FD, χ^2_{13} and χ^2_{21} vorticity calculation methods are found to produce a smaller vorticity random error compared to the FD and χ^2_9 vorticity calculation methods for the same experimental conditions. This occurs at the expense of additional underestimation of vorticity in the peak vorticity regions. The analytical results developed in this paper can be used to predict *a priori* the random error component in the out-of-plane vorticity given the random velocity error or conversely for a desired accuracy in the vorticity the required error bounds on velocity and velocity sampling separation can be estimated. The bias error in a physical experiment can also be estimated given the velocity sampling separation and an estimate of the expected vortex length scale using equations which are based on a local Oseen Vortex model. These equations can also be used to estimate the required spatial velocity sampling separation for a desired bound on the bias error.

A major conclusion of this study is that the requirements to minimise the random error and to minimise the bias error cannot be satisfied simultaneously, as both effects are coupled and oppose each other. The coupling parameter is the non-dimensional velocity sampling separation. Increasing the velocity sampling separation decreases the random vorticity error but increase the bias error and visa versa.

The χ^2_{21} vorticity calculation method is the preferred choice for the vorticity calculation method. This method has a random error transmission factor similar to that of the AGW-FD vorticity calculation method and provides the lowest random error transmission for a given velocity sampling separation. At the same time, the χ^2_{21} vorticity calculation method has a bias error which is considerably smaller than the AGW-FD vorticity calculation method.

The other possible method for reducing the random vorticity error is to reduce the random velocity error. If small velocity random errors can be achieved in the velocity measurements, then the FD and χ^2_9 vorticity calculation methods are preferable, as they produce the smallest bias error. However, the one point which needs to be kept in mind, is that these two methods will also produce significant vorticity bias errors, which can be substantially larger than the random vorticity error, if great care is not exercised in the selection of the velocity sampling separation.

A physical experiment of a laminar vortex ring in which the in-plane velocity is measured using CCDPIV, has been used to illustrate the application of the results and procedures developed in this paper and to provide further supporting evidence of these results. An important conclusion from these physical experiments is that all vorticity calculation methods produced the same circulation around the vortex ring, provided the integration box was large enough to capture the entire vorticity of the ring. However, for smaller integration circuits the bias problem due to lack of velocity sampling separation is still present, even in the circulation calculation using the velocity integration method. This point is probably not well known.

References

Adrian R (1986) Multi-point optical mesurements of simultaneous vectors in unsteady flow – a review. Int J Heat Fluid Flow 7: 127–145

Adrian R; Yao C (1985) Pulsed laser technique application to liquid and gaseous flows and the scattering power of seed materials. Appl Opt 24: 44–52

Agui J; Jimenes J (1987) On the performance of particle tracking. J Fluid Mech 185: 447–468

Arroyo M; Saviron J (1992) Rayleigh-bernard convection in a small box: spatial features and thermal dependence of the velocity field. J Fluid Mech 235: 325–348

Baker D; Fourney M (1977) Measuring fluid velocities with speckle patterns. Opt Lett 1: 135–137

Dimotakis P; Debussy F; Koochesfahani M (1981) Particle streak velocity field measurements in a two-dimensional mixing layer. Phys Fluids 24: 995–999

Glezer A; Coles D (1990) An experimental study of a turbulent vortex ring. J Fluid Mech 211: 243–283

Graham L; Soria J (1994) A study of an inclined cylinder wake using digital particle image velocimetry. In: 7th Int Symp on Applications of Laser Techniques to Fluid Mechanics Lisbon, Portugal

Imaichi K; Ohmi K (1983) Numerical processing of flow-visualisation pictures – measurement of two-dimensional vortex flow. J Fluid Mech 129: 283–311

Moffat R (1988) Describing the uncertainties in experimental results. Exp Thermal Fluid Sci 1: 3–17

Press W; Teukolsky S; Vetterling W; Flannery BP (1989) Numerical Recipes in C. Cambridge University Press, Cambridge

Saffman P (1995) Vortex Dynamics. Cambridge University Press, Cambridge

Shepherd RF; LaFontaine RF; Welch, LW; Soria J; Pearson IG (1991) Measurement of instantaneous flows using particle image velocimetry. In 2nd World Conf on Experimental Heat Transfer, Fluid Mechanics and Thermodynamics Dubrovnik, Yugoslavia

Simpkins PG; Dudderar TD (1978) Laser speckle measurement in transient bernard convection. J Fluid Mech 89: 665–671

Sinha S; Kuhlman P (1992) Investigating the use of stereoscopic particle streak velocimetry for estimating the three-dimensional vorticity field. Exp Fluids 12: 377–384

Soria J (1996) An investigation of the near wake of a circular cylinder using a video-based digital cross-correlation particle image velocimetry technique. Exp Thermal Fluid Sci 12: 221–233

Spedding G; Rignot E (1993) Performance analysis and application of grid interpolation techniques for fluid flows. Exp Fluids 15: 417–430

Willert CE; Gharib M (1991) Digital particle image velocimetry. Exp Fluids 10: 181–193

Wu J; Sheridan J; Soria J; Welsh MC (1994) An investigation of unsteady flow behind a circular cylinder using a digital piv method. In Laser Anemometry – 1994: Advances and Applications ASME FED-Vol 191, pp 167–172